The Variability of the Black Hole Image in M87 at the Dynamical Timescale

(article starts on next page)

CrossMark

The Variability of the Black Hole Image in M87 at the Dynamical Timescale

Kaushik Satapathy[1,2], Dimitrios Psaltis[1], Feryal Özel[1], Lia Medeiros[3,127], Sean T. Dougall[1], Chi-Kwan Chan[1],
Maciek Wielgus[4,5], Ben S. Prather[6], George N. Wong[6], Charles F. Gammie[6,7], Kazunori Akiyama[4,8,9],
Antxon Alberdi[10], Walter Alef[11], Juan Carlos Algaba[12], Richard Anantua[4,5], Keiichi Asada[13], Rebecca Azulay[11,14,15],
Anne-Kathrin Baczko[11], David Ball[16], Mislav Balokovic[4,5], John Barrett[8], Bradford A. Benson[17,18], Dan Bintley[19],
Lindy Blackburn[4,5], Raymond Blundell[5], Wilfred Boland[20], Katherine L. Bouman[4,5,21], Geoffrey C. Bower[22],
Hope Boyce[23,24], Michael Bremer[25], Christiaan D. Brinkerink[26], Roger Brissenden[4,5], Silke Britzen[11],
Avery E. Broderick[27,28,29], Dominique Broguiere[25], Thomas Bronzwaer[26], Sandra Bustamente[30], Do-Young Byun[31,32],
John E. Carlstrom[18,33,34,35], Andrew Chael[36,128], Koushik Chatterjee[37], Shami Chatterjee[38], Ming-Tang Chen[22],
Yongjun Chen (陈永军)[39,40], Ilje Cho[31,32], Pierre Christian[41], John E. Conway[42], James M. Cordes[38],
Thomas M. Crawford[18,33], Geoffrey B. Crew[8], Alejandro Cruz-Osorio[43], Yuzhu Cui[44,45], Jordy Davelaar[26,46,47],
Mariafelicia De Laurentis[43,48,49], Roger Deane[50,51,52], Jessica Dempsey[19], Gregory Desvignes[53], Jason Dexter[54],
Sheperd S. Doeleman[4,5], Ralph P. Eatough[11,55], Heino Falcke[26], Joseph Farah[4,5,56], Vincent L. Fish[8], Ed Fomalont[57],
H. Alyson Ford[16], Raquel Fraga-Encinas[26], Per Friberg[19], Christian M. Fromm[4,5,43], Antonio Fuentes[10],
Peter Galison[4,58,59], Roberto García[25], Olivier Gentaz[25], Boris Georgiev[28,29], Ciriaco Goddi[26,60], Roman Gold[27,61],
Arturo I. Gómez-Ruiz[62,63], José L. Gómez[64], Minfeng Gu (顾敏峰)[39,65], Mark Gurwell[5], Kazuhiro Hada[44,45],
Daryl Haggard[23,24], Michael H. Hecht[8], Ronald Hesper[66], Luis C. Ho (何子山)[67,68], Paul Ho[13], Mareki Honma[44,45,69],
Chih-Wei L. Huang[13], Lei Huang (黄磊)[39,65], David H. Hughes[62], Shiro Ikeda[9,70,71,72], Makoto Inoue[13], Sara Issaoun[26],
David J. James[4,5], Buell T. Jannuzi[16], Michael Janssen[11], Britton Jeter[28,29], Wu Jiang (江悟)[39],
Alejandra Jimenez-Rosales[26], Michael D. Johnson[4,5], Svetlana Jorstad[73,74], Taehyun Jung[31,32], Mansour Karami[27,28],
Ramesh Karuppusamy[11], Tomohisa Kawashima[75], Garrett K. Keating[5], Mark Kettenis[76], Dong-Jin Kim[11],
Jae-Young Kim[11,31], Jongsoo Kim[31], Junhan Kim[16,21], Motoki Kino[9,77], Jun Yi Koay[13], Yutaro Kofuji[44,69],
Patrick M. Koch[13], Shoko Koyama[13,78], Carsten Kramer[25], Michael Kramer[11], Thomas P. Krichbaum[11],
Cheng-Yu Kuo[13,79], Tod R. Lauer[80], Sang-Sung Lee[31], Aviad Levis[21], Yan-Rong Li (李彦荣)[81], Zhiyuan Li
(李志远)[82,83], Michael Lindqvist[42], Rocco Lico[10,11], Greg Lindahl[5], Jun Liu (刘俊)[11], Kuo Liu[11],
Elisabetta Liuzzo[84], Wen-Ping Lo[13,85], Andrei P. Lobanov[11], Laurent Loinard[86,87], Colin Lonsdale[8], Ru-Sen Lu
(路如森)[11,88,89], Nicholas R. MacDonald[11], Jirong Mao (毛基荣)[90,91,92], Nicola Marchili[11,84], Sera Markoff[37,93],
Daniel P. Marrone[16], Alan P. Marscher[73], Iván Martí-Vidal[14,15], Satoki Matsushita[13], Lynn D. Matthews[8],
Karl M. Menten[11], Izumi Mizuno[19], Yosuke Mizuno[43,94], James M. Moran[4,5], Kotaro Moriyama[8,44],
Monika Moscibrodzka[26], Cornelia Müller[11,26], Alejandro Mus Mejías[14,15], Gibwa Musoke[26,37], Hiroshi Nagai[9,45],
Neil M. Nagar[95], Masanori Nakamura[13,96], Ramesh Narayan[4,5], Gopal Narayanan[30], Iniyan Natarajan[50,52,97],
Antonios Nathanail[43], Joey Neilsen[98], Roberto Neri[25], Chunchong Ni[28,29], Aristeidis Noutsos[11], Michael A. Nowak[99],
Hiroki Okino[44,69], Héctor Olivares[26], Gisela N. Ortiz-León[11], Tomoaki Oyama[44], Daniel C. M. Palumbo[4,5],
Jongho Park[13,129], Nimesh Patel[5], Ue-Li Pen[27,100,101,102], Dominic W. Pesce[4,5], Vincent Piétu[25], Richard Plambeck[103],
Aleksandar PopStefanija[30], Oliver Porth[37,43], Felix M. Pötzl[11], Jorge A. Preciado-López[27], Hung-Yi Pu[13,27,104],
Venkatessh Ramakrishnan[95], Ramprasad Rao[22], Mark G. Rawlings[19], Alexander W. Raymond[4,5],
Luciano Rezzolla[43,105,106], Bart Ripperda[47,107], Freek Roelofs[5,26], Alan Rogers[8], Eduardo Ros[11], Mel Rose[16],
Arash Roshanineshat[16], Helge Rottmann[11], Alan L. Roy[11], Chet Ruszczyk[8], Kazi L. J. Rygl[84], Salvador Sánchez[108],
David Sánchez-Arguelles[62,109], Mahito Sasada[44,110], Tuomas Savolainen[11,111,112], F. Peter Schloerb[30],
Karl-Friedrich Schuster[25], Lijing Shao[11,68], Zhiqiang Shen (沈志强)[39,40], Des Small[76], Bong Won Sohn[31,32,113],
Jason SooHoo[8], He Sun (孙赫)[21], Fumie Tazaki[44], Alexandra J. Tetarenko[19], Paul Tiede[28,29],
Remo P. J. Tilanus[16,26,114,115], Michael Titus[8], Kenji Toma[116,117], Pablo Torne[11,108], Efthalia Traianou[11],
Tyler Trent[16], Sascha Trippe[118], Ilse van Bemmel[76], Huib Jan van Langevelde[76,119], Daniel R. van Rossum[26],
Jan Wagner[11], Derek Ward-Thompson[120], John Wardle[121], Jonathan Weintroub[4,5], Norbert Wex[11],
Robert Wharton[11], Kaj Wiik[122], Qingwen Wu (吴庆文)[123], Doosoo Yoon[37], André Young[26], Ken Young[5],
Ziri Younsi[43,124], Feng Yuan (袁峰)[39,65,125], Ye-Fei Yuan (袁业飞)[126], J. Anton Zensus[11], Guang-Yao Zhao[10], and
Shan-Shan Zhao[39]

[1] Astronomy Department, University of Arizona, 933 N. Cherry Ave, Tucson, AZ 85721, USA
[2] Department of Physics, University of Arizona, 1118 E 4th St, Tucson, AZ 85721, USA
[3] School of Natural Sciences, Institute for Advanced Study, 1 Einstein Drive, Princeton, NJ 08540, USA
[4] Black Hole Initiative at Harvard University, 20 Garden Street, Cambridge, MA 02138, USA
[5] Center for Astrophysics, Harvard & Smithsonian, 60 Garden Street, Cambridge, MA 02138, USA
[6] Illinois Center for Advanced Studies of the Universe, Department of Physics, University of Illinois, 1110 West Green Street, Urbana, IL 61801, USA
[7] Department of Astronomy, University of Illinois, 1002 West Green Street, Urbana, IL 61801, USA
[8] Massachusetts Institute of Technology Haystack Observatory, 99 Millstone Road, Westford, MA 01886, USA
[9] National Astronomical Observatory of Japan, 2-21-1 Osawa, Mitaka, Tokyo 181-8588, Japan
[10] Instituto de Astrofísica de Andalucía-CSIC, Glorieta de la Astronomía s/n, E-18008 Granada, Spain

[11] Max-Planck-Institut für Radioastronomie, Auf dem Hügel 69, D-53121 Bonn, Germany

[12] Department of Physics, Faculty of Science, University of Malaya, 50603 Kuala Lumpur, Malaysia

[13] Institute of Astronomy and Astrophysics, Academia Sinica, 11F of Astronomy-Mathematics Building, AS/NTU No. 1, Sec. 4, Roosevelt Rd, Taipei 10617, Taiwan, R.O.C.

[14] Departament d'Astronomia i Astrofísica, Universitat de València, C. Dr. Moliner 50, E-46100 Burjassot, València, Spain

[15] Observatori Astronòmic, Universitat de València, C. Catedrático José Beltrán 2, E-46980 Paterna, València, Spain

[16] Steward Observatory and Department of Astronomy, University of Arizona, 933 N. Cherry Ave., Tucson, AZ 85721, USA

[17] Fermi National Accelerator Laboratory, MS209, P.O. Box 500, Batavia, IL 60510, USA

[18] Department of Astronomy and Astrophysics, University of Chicago, 5640 South Ellis Avenue, Chicago, IL 60637, USA

[19] East Asian Observatory, 660 N. A'ohoku Place, Hilo, HI 96720, USA

[20] Nederlandse Onderzoekschool voor Astronomie (NOVA), PO Box 9513, 2300 RA Leiden, The Netherlands

[21] California Institute of Technology, 1200 East California Boulevard, Pasadena, CA 91125, USA

[22] Institute of Astronomy and Astrophysics, Academia Sinica, 645 N. A'ohoku Place, Hilo, HI 96720, USA

[23] Department of Physics, McGill University, 3600 rue University, Montréal, QC, H3A 2T8, Canada

[24] McGill Space Institute, McGill University, 3550 rue University, Montréal, QC, H3A 2A7, Canada

[25] Institut de Radioastronomie Millimétrique, 300 rue de la Piscine, F-38406 Saint Martin d'Hères, France

[26] Department of Astrophysics, Institute for Mathematics, Astrophysics and Particle Physics (IMAPP), Radboud University, P.O. Box 9010, 6500 GL Nijmegen, The Netherlands

[27] Perimeter Institute for Theoretical Physics, 31 Caroline Street North, Waterloo, ON, N2L 2Y5, Canada

[28] Department of Physics and Astronomy, University of Waterloo, 200 University Avenue West, Waterloo, ON, N2L 3G1, Canada

[29] Waterloo Centre for Astrophysics, University of Waterloo, Waterloo, ON, N2L 3G1, Canada

[30] Department of Astronomy, University of Massachusetts, Amherst, MA 01003, USA

[31] Korea Astronomy and Space Science Institute, Daedeok-daero 776, Yuseong-gu, Daejeon 34055, Republic of Korea

[32] University of Science and Technology, Gajeong-ro 217, Yuseong-gu, Daejeon 34113, Republic of Korea

[33] Kavli Institute for Cosmological Physics, University of Chicago, 5640 South Ellis Avenue, Chicago, IL 60637, USA

[34] Department of Physics, University of Chicago, 5720 South Ellis Avenue, Chicago, IL 60637, USA

[35] Enrico Fermi Institute, University of Chicago, 5640 South Ellis Avenue, Chicago, IL 60637, USA

[36] Princeton Center for Theoretical Science, Jadwin Hall, Princeton University, Princeton, NJ 08544, USA

[37] Anton Pannekoek Institute for Astronomy, University of Amsterdam, Science Park 904, 1098 XH, Amsterdam, The Netherlands

[38] Cornell Center for Astrophysics and Planetary Science, Cornell University, Ithaca, NY 14853, USA

[39] Shanghai Astronomical Observatory, Chinese Academy of Sciences, 80 Nandan Road, Shanghai 200030, People's Republic of China

[40] Key Laboratory of Radio Astronomy, Chinese Academy of Sciences, Nanjing 210008, People's Republic of China

[41] Physics Department, Fairfield University, 1073 North Benson Road, Fairfield, CT 06824, USA

[42] Department of Space, Earth and Environment, Chalmers University of Technology, Onsala Space Observatory, SE-43992 Onsala, Sweden

[43] Institut für Theoretische Physik, Goethe-Universität Frankfurt, Max-von-Laue-Straße 1, D-60438 Frankfurt am Main, Germany

[44] Mizusawa VLBI Observatory, National Astronomical Observatory of Japan, 2-12 Hoshigaoka, Mizusawa, Oshu, Iwate 023-0861, Japan

[45] Department of Astronomical Science, The Graduate University for Advanced Studies (SOKENDAI), 2-21-1 Osawa, Mitaka, Tokyo 181-8588, Japan

[46] Department of Astronomy and Columbia Astrophysics Laboratory, Columbia University, 550 W 120th Street, New York, NY 10027, USA

[47] Center for Computational Astrophysics, Flatiron Institute, 162 Fifth Avenue, New York, NY 10010, USA

[48] Dipartimento di Fisica "E. Pancini,"Universitá di Napoli "Federico II", Compl. Univ. di Monte S. Angelo, Edificio G, Via Cinthia, I-80126, Napoli, Italy

[49] INFN Sez. di Napoli, Compl. Univ. di Monte S. Angelo, Edificio G, Via Cinthia, I-80126, Napoli, Italy

[50] Wits Centre for Astrophysics, University of the Witwatersrand, 1 Jan Smuts Avenue, Braamfontein, Johannesburg 2050, South Africa

[51] Department of Physics, University of Pretoria, Hatfield, Pretoria 0028, South Africa

[52] Centre for Radio Astronomy Techniques and Technologies, Department of Physics and Electronics, Rhodes University, Makhanda 6140, South Africa

[53] LESIA, Observatoire de Paris, Université PSL, CNRS, Sorbonne Université, Université de Paris, 5 place Jules Janssen, F-92195 Meudon, France

[54] JILA and Department of Astrophysical and Planetary Sciences, University of Colorado, Boulder, CO 80309, USA

[55] National Astronomical Observatories, Chinese Academy of Sciences, 20A Datun Road, Chaoyang District, Beijing 100101, People's Republic of China

[56] University of Massachusetts Boston, 100 William T. Morrissey Boulevard, Boston, MA 02125, USA

[57] National Radio Astronomy Observatory, 520 Edgemont Rd, Charlottesville, VA 22903, USA

[58] Department of History of Science, Harvard University, Cambridge, MA 02138, USA

[59] Department of Physics, Harvard University, Cambridge, MA 02138, USA

[60] INAF—Osservatorio Astronomico di Cagliari, Via della Scienza 5, I-09047, Selargius, CA, Italy

[61] CP3-Origins, University of Southern Denmark, Campusvej 55, DK-5230 Odense M, Denmark

[62] Instituto Nacional de Astrofísica, Óptica y Electrónica. Apartado Postal 51 y 216, 72000. Puebla Pue., México

[63] Consejo Nacional de Ciencia y Tecnologìa, Av. Insurgentes Sur 1582, 03940, Ciudad de México, México

[64] Instituto de Astrofísica de Andalucía-CíSIC, Glorieta de la Astronomía s/n, E-18008 Granada, Spain

[65] Key Laboratory for Research in Galaxies and Cosmology, Chinese Academy of Sciences, Shanghai 200030, People's Republic of China

[66] NOVA Sub-mm Instrumentation Group, Kapteyn Astronomical Institute, University of Groningen, Landleven 12, 9747 AD Groningen, The Netherlands

[67] Department of Astronomy, School of Physics, Peking University, Beijing 100871, People's Republic of China

[68] Kavli Institute for Astronomy and Astrophysics, Peking University, Beijing 100871, People's Republic of China

[69] Department of Astronomy, Graduate School of Science, The University of Tokyo, 7-3-1 Hongo, Bunkyo-ku, Tokyo 113-0033, Japan

[70] The Institute of Statistical Mathematics, 10-3 Midori-cho, Tachikawa, Tokyo, 190-8562, Japan

[71] Department of Statistical Science, The Graduate University for Advanced Studies (SOKENDAI), 10-3 Midori-cho, Tachikawa, Tokyo 190-8562, Japan

[72] Kavli Institute for the Physics and Mathematics of the Universe, The University of Tokyo, 5-1-5 Kashiwanoha, Kashiwa, 277-8583, Japan

[73] Institute for Astrophysical Research, Boston University, 725 Commonwealth Ave., Boston, MA 02215, USA

[74] Astronomical Institute, St. Petersburg University, Universitetskij pr., 28, Petrodvorets, 198504 St. Petersburg, Russia

[75] Institute for Cosmic Ray Research, The University of Tokyo, 5-1-5 Kashiwanoha, Kashiwa, Chiba 277-8582, Japan

[76] Joint Institute for VLBI ERIC (JIVE), Oude Hoogeveensedijk 4, 7991 PD Dwingeloo, The Netherlands

[77] Kogakuin University of Technology & Engineering, Academic Support Center, 2665-1 Nakano, Hachioji, Tokyo 192-0015, Japan

[78] Niigata University, 8050 Ikarashi-nino-cho, Nishi-ku, Niigata 950-2181, Japan

[79] Physics Department, National Sun Yat-Sen University, No. 70, Lien-Hai Road, Kaosiung City 80424, Taiwan, R.O.C.

[80] National Optical Astronomy Observatory, 950 N. Cherry Ave., Tucson, AZ 85719, USA

[81] Key Laboratory for Particle Astrophysics, Institute of High Energy Physics, Chinese Academy of Sciences, 19B Yuquan Road, Shijingshan District, Beijing, People's Republic of China

[82] School of Astronomy and Space Science, Nanjing University, Nanjing 210023, People's Republic of China

[83] Key Laboratory of Modern Astronomy and Astrophysics, Nanjing University, Nanjing 210023, People's Republic of China

[84] Italian ALMA Regional Centre, INAF-Istituto di Radioastronomia, Via P. Gobetti 101, I-40129 Bologna, Italy

[85] Department of Physics, National Taiwan University, No.1, Sect. 4, Roosevelt Rd., Taipei 10617, Taiwan, R.O.C

[86] Instituto de Radioastronomía y Astrofísica, Universidad Nacional Autónoma de México, Morelia 58089, México

[87] Instituto de Astronomía, Universidad Nacional Autónoma de México, CdMx 04510, México

[88] Shanghai Astronomical Observatory, Chinese Academy of Sciences, 80 Nandan Road, Shanghai 200030, People's Republic of China

[89] Key Laboratory of Radio Astronomy, Chinese Academy of Sciences, Nanjing 210008, People's Republic of China

[90] Yunnan Observatories, Chinese Academy of Sciences, 650011 Kunming, Yunnan Province, People's Republic of China

[91] Center for Astronomical Mega-Science, Chinese Academy of Sciences, 20A Datun Road, Chaoyang District, Beijing, 100012, People's Republic of China

[92] Key Laboratory for the Structure and Evolution of Celestial Objects, Chinese Academy of Sciences, 650011 Kunming, People's Republic of China

[93] Gravitation Astroparticle Physics Amsterdam (GRAPPA) Institute, University of Amsterdam, Science Park 904, 1098 XH Amsterdam, The Netherlands

[94] Tsung-Dao Lee Institute and School of Physics and Astronomy, Shanghai Jiao Tong University, Shanghai, 200240, People's Republic of China

[95] Astronomy Department, Universidad de Concepción, Casilla 160-C, Concepción, Chile

[96] National Institute of Technology, Hachinohe College, 16-1 Uwanotai, Tamonoki, Hachinohe City, Aomori 039-1192, Japan

[97] South African Radio Astronomy Observatory, Observatory 7925, Cape Town, South Africa

[98] Villanova University, Mendel Science Center Rm. 263B, 800 E Lancaster Ave, Villanova, PA 19085, USA

[99] Physics Department, Washington University CB 1105, St Louis, MO 63130, USA

[100] Canadian Institute for Theoretical Astrophysics, University of Toronto, 60 St. George Street, Toronto, ON, M5S 3H8, Canada

[101] Dunlap Institute for Astronomy and Astrophysics, University of Toronto, 50 St. George Street, Toronto, ON, M5S 3H4, Canada

[102] Canadian Institute for Advanced Research, 180 Dundas St West, Toronto, ON, M5G 1Z8, Canada

[103] Radio Astronomy Laboratory, University of California, Berkeley, CA 94720, USA

[104] Department of Physics, National Taiwan Normal University, No. 88, Sec. 4, Tingzhou Rd., Taipei 116, Taiwan, R.O.C.

[105] Frankfurt Institute for Advanced Studies, Ruth-Moufang-Strasse 1, D-60438 Frankfurt, Germany

[106] School of Mathematics, Trinity College, Dublin 2, Ireland

[107] Department of Astrophysical Sciences, Peyton Hall, Princeton University, Princeton, NJ 08544, USA

[108] Instituto de Radioastronomía Milimétrica, IRAM, Avenida Divina Pastora 7, Local 20, E-18012, Granada, Spain

[109] Consejo Nacional de Ciencia y Tecnología, Av. Insurgentes Sur 1582, 03940, Ciudad de México, México

[110] Hiroshima Astrophysical Science Center, Hiroshima University, 1-3-1 Kagamiyama, Higashi-Hiroshima, Hiroshima 739-8526, Japan

[111] Aalto University Department of Electronics and Nanoengineering, PL 15500, FI-00076 Aalto, Finland

[112] Aalto University Metsähovi Radio Observatory, Metsähovintie 114, FI-02540 Kylmälä, Finland

[113] Department of Astronomy, Yonsei University, Yonsei-ro 50, Seodaemun-gu, 03722 Seoul, Republic of Korea

[114] Leiden Observatory—Allegro, Leiden University, P.O. Box 9513, 2300 RA Leiden, The Netherlands

[115] Netherlands Organisation for Scientific Research (NWO), Postbus 93138, 2509 AC Den Haag, The Netherlands

[116] Frontier Research Institute for Interdisciplinary Sciences, Tohoku University, Sendai 980-8578, Japan

[117] Astronomical Institute, Tohoku University, Sendai 980-8578, Japan

[118] Department of Physics and Astronomy, Seoul National University, Gwanak-gu, Seoul 08826, Republic of Korea

[119] Leiden Observatory, Leiden University, Postbus 2300, 9513 RA Leiden, The Netherlands

[120] Jeremiah Horrocks Institute, University of Central Lancashire, Preston, PR1 2HE, UK

[121] Physics Department, Brandeis University, 415 South Street, Waltham, MA 02453, USA

[122] Tuorla Observatory, Department of Physics and Astronomy, University of Turku, Finland

[123] School of Physics, Huazhong University of Science and Technology, Wuhan, Hubei, 430074, People's Republic of China

[124] Mullard Space Science Laboratory, University College London, Holmbury St. Mary, Dorking, Surrey, RH5 6NT, UK

[125] School of Astronomy and Space Sciences, University of Chinese Academy of Sciences, No. 19A Yuquan Road, Beijing 100049, People's Republic of China

[126] Astronomy Department, University of Science and Technology of China, Hefei 230026, People's Republic of China

Abstract

The black hole images obtained with the Event Horizon Telescope (EHT) are expected to be variable at the dynamical timescale near their horizons. For the black hole at the center of the M87 galaxy, this timescale (5–61 days) is comparable to the 6 day extent of the 2017 EHT observations. Closure phases along baseline triangles are robust interferometric observables that are sensitive to the expected structural changes of the images but are free of station-based atmospheric and instrumental errors. We explored the day-to-day variability in closure-phase measurements on all six linearly independent nontrivial baseline triangles that can be formed from the 2017 observations. We showed that three triangles exhibit very low day-to-day variability, with a dispersion of $\sim 3°–5°$. The only triangles that exhibit substantially higher variability ($\sim 90°–180°$) are the ones with baselines that cross the visibility amplitude minima on the u–v plane, as expected from theoretical modeling. We used two sets of general relativistic magnetohydrodynamic simulations to explore the dependence of the predicted variability on various black hole and accretion-flow parameters. We found that changing the magnetic field configuration, electron temperature model, or black hole spin has a marginal effect on the model consistency with the observed level of variability. On the other hand, the most discriminating image characteristic of models is the fractional width of the bright ring of emission. Models that best reproduce the observed small level of variability are characterized by thin ring-like images with structures dominated by gravitational lensing effects and thus least affected by turbulence in the accreting plasmas.

Unified Astronomy Thesaurus concepts: Black hole physics (159); High energy astrophysics (739)

---

[127] NSF Astronomy and Astrophysics Postdoctoral Fellow.

[128] NASA Hubble Fellowship Program, Einstein Fellow.

[129] EACOA fellow.

1. Introduction

The Event Horizon Telescope (EHT) has produced horizon-scale images of the black hole in the center of the M87 galaxy using Very Long Baseline Interferometry (VLBI) at a wavelength of 1.3 mm (EHT Collaboration et al. 2019a, 2019b, 2019c, 2019d, 2019e, 2019f). Together with upcoming studies

of the black hole in the center of the Milky Way, Sgr A*, these images have opened up numerous avenues to studying physics at event-horizon scales related to both accretion processes and gravity. The structure of the accretion disks and jets observed around the black holes will improve our understanding of the behavior of plasma in these environments (EHT Collaboration et al. 2019e, 2019f). The measurements of the sizes and shapes of the black hole shadows give insights into deviations of the black hole spacetime from the Kerr metric (Psaltis 2019; Psaltis et al.2020).

Accretion flows, which make up the horizon-scale environments of black holes, are expected to be highly variable by nature. The radiation observed from these regions at 1.3 mm is dominated by synchrotron emission from electrons that are heated and accelerated by magnetohydrodynamic turbulence (EHT Collaboration et al. 2019e). The accretion flow is also expected to evolve at the dynamical timescales near the innermost stable circular orbit (ISCO), which range from 4 to 56 minutes for Sgr A* (for $M_{BH} = 4.148 \times 10^6 M_\odot$; see Gravity Collaboration et al. 2019) and 5 to 61 days for M87 (depending on the black hole spin; Bardeen et al. 1972). The timescales suggest that there can be substantial variability in the source structure over a single observing night for Sgr A*, which makes it difficult to obtain a static image. However, we expect substantial source variability in M87 only for observations that span about a week or longer. Evidence for long-term variability in the image structure of M87 has been reported recently, based on VLBI observations spanning nearly a decade (Wielgus & The EHT Collaboration 2020).

The EHT observed M87 in 2017 April for four nights with a maximum separation of six calendar days between observations. For a black hole of the inferred mass ($M_{BH} = 6.5 \times 10^9 M_\odot$; Gebhardt et al. 2011; EHT Collaboration et al. 2019f), the six days correspond to $16\,GM/c^3$. This is approximately equal to ∼3.5 dynamical timescales at the ISCO for a maximally spinning black hole. Over this observation span, only a limited amount of variability in source structure was inferred between days, reflected as a small change in the thickness or azimuthal brightness distribution of the observed bright emission ring (EHT Collaboration et al. 2019d).

Our goal in this paper is to use general relativistic magnetohydrodynamic (GRMHD) simulations of accretion flows, followed by general relativistic ray tracing and radiative transfer, with parameters that are relevant to the M87 black hole, in order to explore the short-term variability in the source structure as it is imprinted in the interferometric observables. The EHT, being an interferometer, measures complex visibilities, which denote the two-dimensional Fourier transform of the source image on the sky. The measurements are typically decomposed into visibility amplitudes and phases (Thompson et al. 2017). Image reconstruction techniques enable us to use these variables and create the map of the source brightness on the plane of the sky (see EHT Collaboration et al. 2019d).

The visibility measurements in VLBI are affected by time-dependent atmospheric and instrumental errors of the telescopes, particularly challenging for the short radio wavelengths (Thompson et al. 2017). The custom-built EHT data reduction pipeline addresses the specific requirements of the millimeter VLBI (EHT Collaboration et al. 2019c). The pipeline uses Atacama Large Millimeter/submillimeter Array (ALMA) as an anchor station, leveraging its extreme sensitivity for the calibration of the entire EHT array (Blackburn et al. 2019; Janssen et al. 2019). As a result, the measured visibilities

indicate sufficient phase-stability to enable long coherent averaging and building up the high signal-to-noise ratio. Remaining station-based errors can be modeled as complex gains multiplying the visibilities. In order to eliminate the effects of these errors in the data, one can construct closure quantities with amplitudes and phases (Jennison 1958; Kulkarni 1989; Thompson et al. 2017; Blackburn et al. 2020). For a set of three baselines forming a closure triangle, the closure phase is defined as the sum of the measured visibility phases in each of these baselines. This cancels out the station-based phase measurement errors for each station. As a result, the closure phases are optimal and robust probes of the intrinsic structure of the source.

Closure phases have indeed proven to be a powerful tool to study and quantify variability in synthetic data from GRMHD simulations. Medeiros et al. (2018) studied the dependence of variability in closure phases on the orientations and baseline lengths of the closure triangles (see also Roelofs et al. 2017). Triangles that involve large baselines (that probe small length scales in the source image) were shown to have a high degree of variability in closure phases. On the other hand, triangles that involve small baselines (that probe the overall size of the ring and source structure) exhibit less variability. The exception to this rule are triangles involving a baseline close to a deep visibility minimum. The visibility phases in regions of visibility minima are extremely sensitive to minor changes in source structure. This localization of variability in the Fourier space is vital in understanding variability in GRMHD simulations and in observations.

In this paper, we first present a data-driven model to quantify the variability of observed closure phases in the various linearly independent triangles of the M87 observations across the six days of observations in 2017. We apply this algorithm to the 2017 EHT data on M87 and identify three closure triangles that show a remarkably small degree of variability. We then explore the degree of variability produced in a large set of GRMHD simulations, with different magnetic field configurations and prescriptions of the plasma physics, and understand the effects of various model parameters on the variability in the models. Finally, we compare the predictions of the GRMHD simulations to the observations and discuss how the latter constrain the physical properties of the accretion flow in M87.

2. Closure-phase Observations of M87

The EHT measures complex visibilities, given by

$$V(u, v) = \int\int dx\, dy\, I(x, y)\, e^{-2\pi i(ux+vy)}, \qquad (1)$$

where $I(x, y)$ represents the total intensity of radiation at a given spatial location (x, y) on the image plane and (u, v) denote the Fourier frequencies corresponding to the (x, y) coordinates. However, due to atmospheric and instrumental effects, the measured visibilities do not represent the actual visibilities of the source. The measured visibilities are related to the source visibilities through complex *gains*. The measured visibility between the ith and the jth telescopes, $\mathscr{V}_{ij}$, can be written as

$$\mathscr{V}_{ij} = g_i g_j^* V_{ij}, \qquad (2)$$

where g_i and g_j are the complex gains associated with the two telescopes, and the star superscript indicates complex conjugates. We define the closure phase as the argument of the
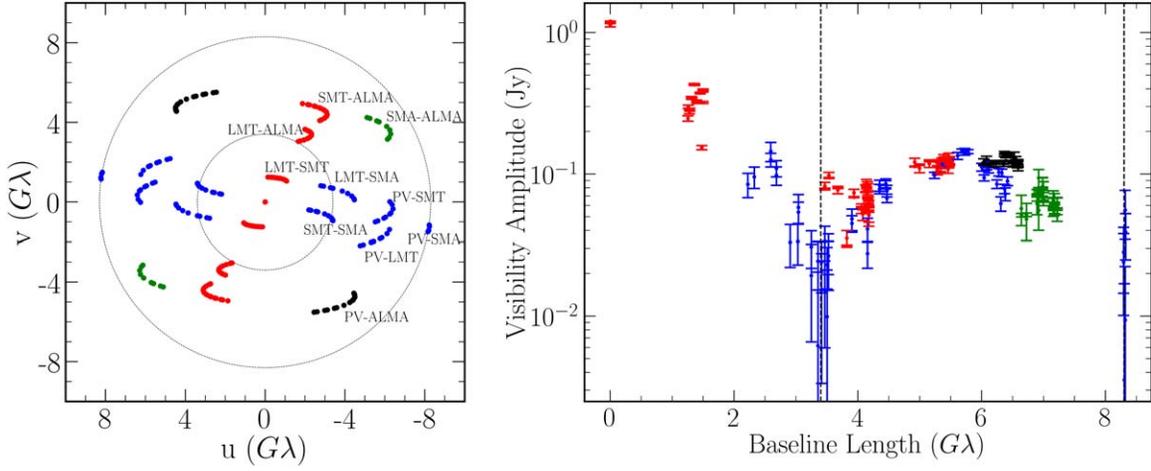
Figure 1. Left: the *u–v* coverage traced by the EHT for the M87 observations on 2017 April 11, with the dashed circles indicating locations of the two observed visibility minima. The colors indicate different orientations of the *u–v* coverage. Right: the visibility amplitude as a function of baseline length on the same day.

complex bispectrum along a closed triangle of three telescopes (Jennison 1958). The closure phase $\phi_{ijk}^{\rm CP}$ for a closure triangle formed by the *i*th, the *j*th, and the *k*th telescopes is hence given by

$$\begin{aligned}
\phi_{ijk}^{\rm CP} &= {\rm Arg}[\mathcal{V}_{ij}\mathcal{V}_{jk}\mathcal{V}_{ki}] \\
&= {\rm Arg}[g_i g_j^* V_{ij} g_j g_k^* V_{jk} g_k g_i^* V_{ki}] \\
&= {\rm Arg}[|g_i|^2 |g_j|^2 |g_k|^2 V_{ij} V_{jk} V_{ki}] \\
&= {\rm Arg}[V_{ij} V_{jk} V_{ki}] \\
&= \phi_{ij} + \phi_{jk} + \phi_{ki},
\end{aligned} \tag{3}$$

where ϕ_{ij} denotes the visibility phase between the *i*th and the *j*th telescopes. Equation (3) shows that the measured closure phase in a triangle is equal to the actual closure phase represented by the source.

The EHT observed M87 on four nights in 2017 April 5, 6, 10, and 11. The observations involved seven stations spread across five geographical locations (EHT Collaboration et al. 2019b): the Atacama Large Millimeter Array (ALMA) and the Atacama Pathfinder Experiment (APEX) in Chile; the James Clerk Maxwell Telescope (JCMT) and the Submillimeter Array (SMA) in Hawaii; the Large Millimeter Telescope (LMT) in Mexico; the Submillimeter Telescope Observatory (SMT) in Arizona; and the IRAM 30 m telescope in Pico Veleta (PV) in Spain. On each night of observation, the rotation of the Earth implies that each baseline traces out an elliptical path in the *u–v* space with the progression of time.

Figure 1 shows the *u–v* coverage for M87 during one of the observing days (left panel) as well as the visibility amplitudes measured as a function of baseline length on the same day (right panel). Two deep minima in visibility amplitude can be seen at baseline lengths of ∼3.4 and ∼8.3 Gλ encountered in three baselines (LMT-SMA, SMT-SMA, and PV-SMA) along the east–west orientation (indicated in blue). In contrast, the minimum encountered by the ALMA-LMT baseline is only marginally deep (right panel of Figure 1).

We construct closure-phase quantities using all the baselines shown in Figure 1. However, closure triangles with two telescopes at the same geographical location yield trivial closure phases, with deviations from zero arising due to changes in the large scale source structure alongside

Table 1
Closure Triangles Used with Baseline Lengths and Inferred Variability in Closure Phases

Triangle[a]	Baseline Lengths (Gλ)[b]			Inferred Variability[c]
	1	2	3	
ALMA-SMA-LMT	6.7–7.2	**3.1–4.5**	**3.4–4.1**	∼30°–60°
ALMA-LMT-SMT	3.4–4.2	1.3–1.5	4.8–5.5	3°.4
ALMA-PV-LMT	6.0–6.6	5.1–6.4	3.4–4.2	4°.6
ALMA-SMA-SMT	6.7–7.2	**2.4–3.5**	4.8–5.5	∼180°
ALMA-PV-SMA	6.0–6.2	**8.2–8.3**	6.8–7.0	…
ALMA-PV-SMT	6.0–6.6	5.5–6.4	5.3–5.5	5°.4

Notes.
[a] The bold baselines indicate the triangles that cross one of the deep visibility minima in the E-W orientation at 3.4 and 8.3 Gλ.
[b] Baselines labeled 1, 2, and 3 in a triangle labeled as A-B-C correspond to the baselines A-B, B-C, and C-A, respectively.
[c] An estimated range of variation in the high-variability triangles, and the maximum likelihood value of the inferred Gaussian variability (Equation (7)) in the low-variability triangles.

systematic and thermal errors (EHT Collaboration et al. 2019c). While these triangles are useful to quantify systematic errors in closure phases, they do not capture any information about the source structure at horizon scales. Hence, we only choose triangles with telescopes at different geographical locations for our study. Since Chile and Hawaii have two stations each, we pick the station with the higher signal-to-noise ratio. We, therefore, consider five stations—ALMA, SMA, LMT, SMT, and PV, out of which six linearly independent closure phases can be constructed. We list the six triangles in Table 1. We choose the triangles such that all of them involve ALMA, which has the highest signal-to-noise ratio, and hence smaller uncertainties in closure-phase measurements.

In Figure 2, we show the evolution of closure phases with time in Greenwich Mean Sidereal Time (GMST) coordinates over all four days of observations in three triangles that exhibit substantial day-to-day variability in closure phases over the span of the 2017 campaign (see also EHT Collaboration et al. 2019c, Section 7.3.2):
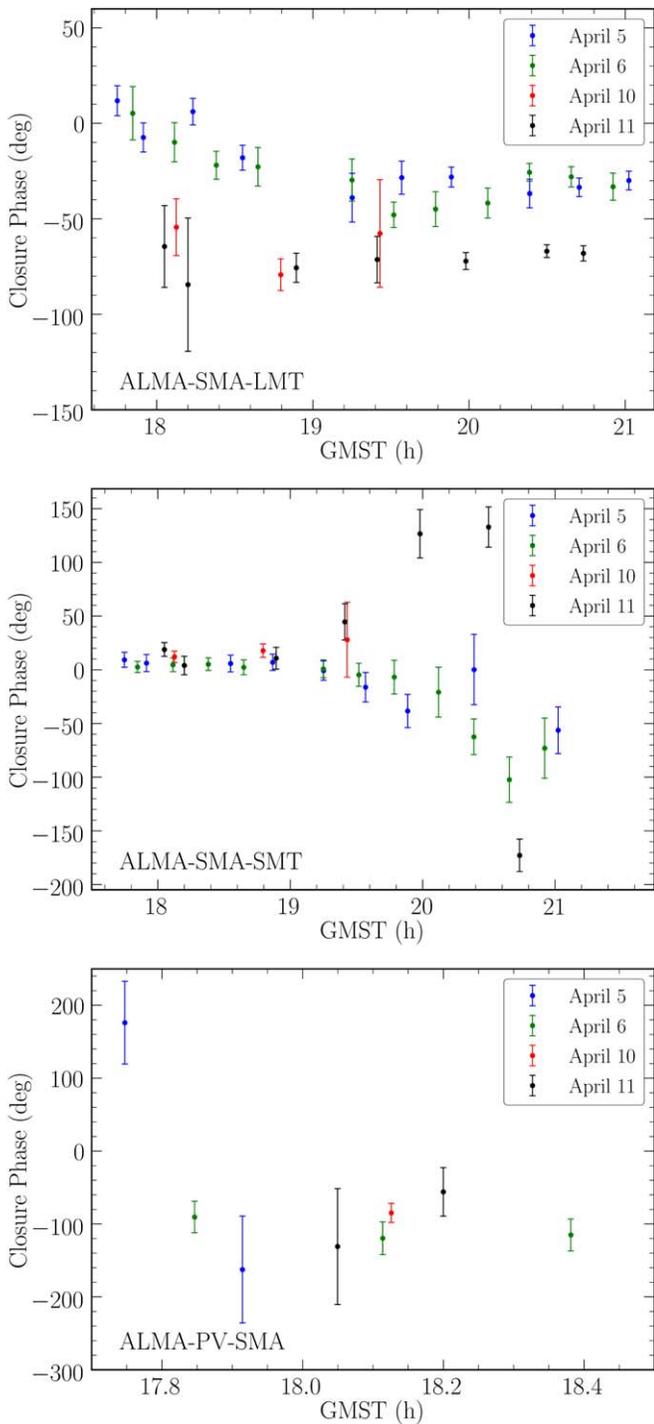
Figure 2. The evolution of closure phases plotted with time for all four days of observation for closure triangles in which baselines are known to encounter regions of deep visibility minima. All three triangles exhibit a high level of variability in closure phases across six days of observation.

(i) The ALMA-SMA-LMT triangle shows a change of 30°–60° between the first two days and the later two days of observation.

(ii) The ALMA-SMA-SMT triangle shows a swing of 180° on each day of observation. In addition to this, the direction of this swing flips between the first two days and the later two days of observation.

(iii) In the ALMA-PV-SMA triangle, it is difficult to quantify the degree of variability because of the reduced

complex visibility amplitudes between PV and SMA baselines, and the low signal-to-noise ratio in some data points. However, a persistent structure in the evolution of closure phases is not observed.

We note that each of these closure triangles involves one of the baselines (i.e., LMT-SMA, SMT-SMA, and PV-SMA) that cross a deep visibility minimum in the E-W orientation. In addition, we note that, in the ALMA-SMA-SMT triangle, the closure phases show little day-to-day variability until ~19 GMST on each day. We attribute this behavior to the fact that the SMT-SMA baseline encounters the deep visibility minimum at ~19 GMST. We plan to analyze the dependence of variability in the observations on the depth of the visibility minima in a future study.

The closure phases in the remaining triangles (i.e., ALMA-LMT-SMT, ALMA-PV-LMT, and ALMA-PV-SMT) show a persistent and continuous evolution with time during each day of observation (see Figure 3). This behavior represents the evolution of closure phases as the various baselines trace their paths on the u–v plane following the rotation of the Earth. However, the same evolution with time is repeated in all days of observations; there is little scatter around the general trend set by the rotation of the baselines. The presence of substantial scatter from day to day would have been a signature of structure variability in the image.

In order to compare the observations to theoretical models, we quantify the degree of closure-phase day-to-day variability observed in this last set of triangles. Upon examination of the closure phases in the maximal set of closure triangles, we find that, outside the set of linearly independent triangles that we choose, only one triangle (LMT-SMT-PV) shows a low degree of day-to-day variability. We conclude that it is optimal and sufficient to quantify the day-to-day variability in the low-variability triangles that we choose in Table 1, since the LMT-SMT-PV triangle can be obtained by a linear combination of these three triangles.

We also note that the comparison between observations and models could, in principle, be carried out for both high-variability and low-variability triangles. However, as we will discuss in Section 4, images from theoretical models uniformly show a high degree of phase variability in baselines that cross a visibility minimum and, as a result, a comparison with the high-variability triangles in the data turns out not to have much discriminating power between various models. The degree of variability exhibited on the low-variability triangles identified in the data, on the other hand, is a more significant challenge to the GRMHD models and proves to be a useful tool to distinguish between them.

The quantification of day-to-day variability in the set of three low-variable triangles is not straightforward, because closure phases evolve with time on each observing day but the individual scans on each day are not aligned at the exact same times. As a result, a difference in closure phases measured in two scans separated by almost (but not exactly) one sidereal day incorporates both the change due to the slightly different locations on the u–v plane probed by the two scans and the change due to the structural changes in the image.

In order to disentangle the two sources of variability, we employ a data-driven analytic model for the evolution of the closure phase with time during a single day of observation. This is meant to capture the change in closure phases introduced by the changing location on the u–v plane of the
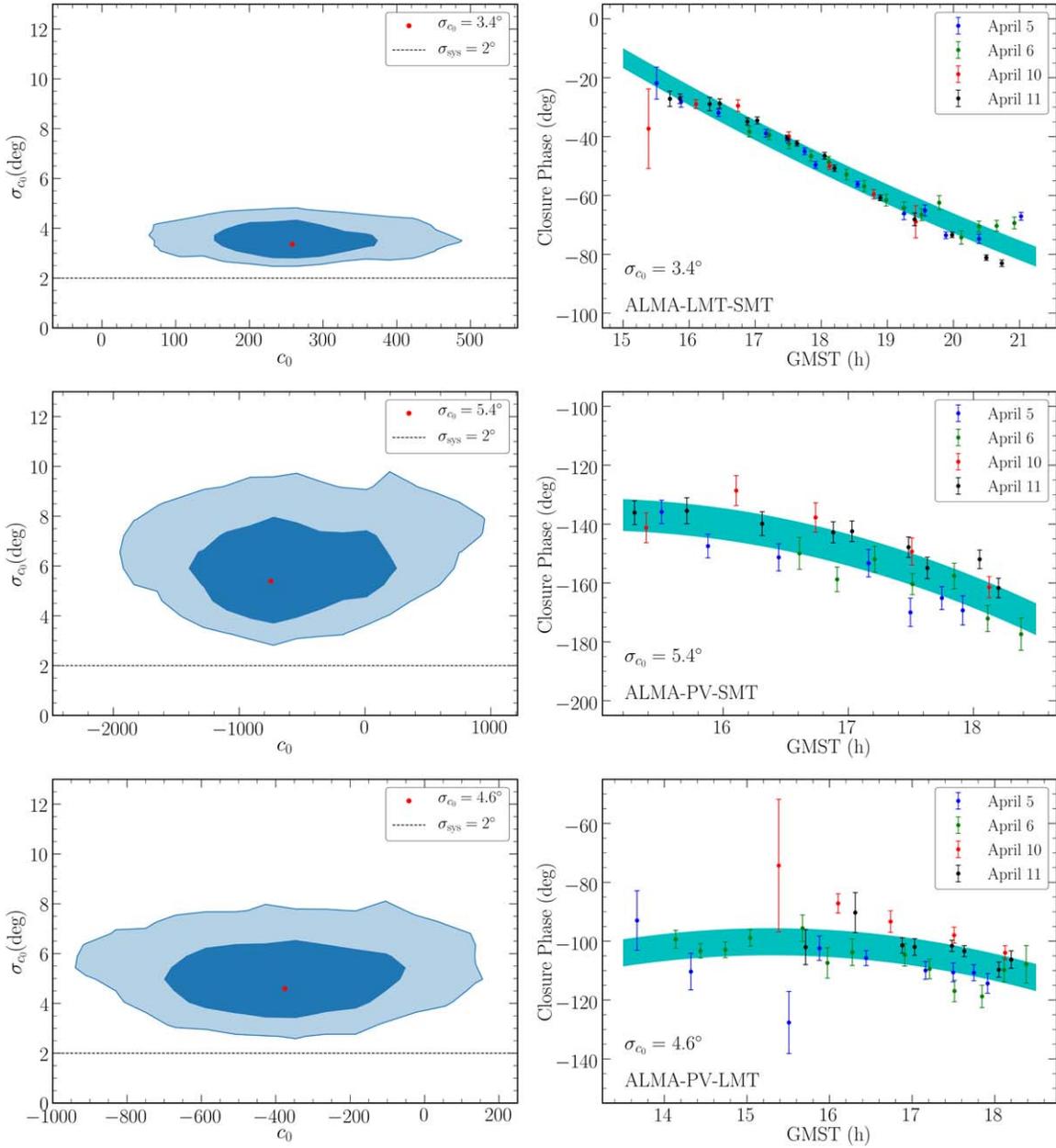
Figure 3. The parameters and functional forms of the data-driven closure-phase evolution model, applied to the closure triangles that exhibit low variability across the six days of 2017 EHT observations (see Equation (4)). Left: the posterior projected on the σ_{c_0}–c_0 parameter plane, where σ_0 is a measure of the variability across the six days. The red dots indicate the most likely values. The contours indicate the levels containing 68% and 95% of the posterior probability. The dashed horizontal lines indicate the systematic error of $2°$ in closure-phase observations. Right: closure-phase observations plotted as a function of time for the same triangles. The cyan band indicates the most likely value of the width of the model σ_{c_0}.

closure triangles. We then compare the overall change of the parameters of this model from day to day, in order to quantify the variability due to structural changes of the image.

For our data-driven model, $\phi_{\text{model}}(t)$, we use a second-order polynomial in the observation time t (in GMST coordinates), given by

$$\phi_{\text{model}}(t) = c_0 + c_1 t + c_2 t^2. \qquad (4)$$

In order to account for potential structural changes from day to day, we allow for an intrinsic Gaussian spread in the zeroth-order coefficient of this polynomial (c_0), with a standard deviation of σ_{c_0}. In this prescription, we do not assign any physical significance to the polynomial coefficients. Since the

maximum separation between any two nights of observations is six days, σ_{c_0} acts as a constraint on the overall change in closure phase at a given time in a given triangle across six days.

Using this model, we define the likelihood of making a particular closure-phase measurement using a Gaussian mixture model as

$$L_i(c_0, c_1, c_2, \sigma_{c_0}) \equiv \left\{ \frac{1}{\sqrt{2\pi(\sigma_i^2 + \sigma_{c_0}^2)}} \right\}$$
$$\times \exp\left[-\frac{1}{2} \frac{\{\phi_i - \phi_{\text{model}}(t_i)\}^2}{(\sigma_i^2 + \sigma_{c_0}^2)} \right], \qquad (5)$$

where ϕ_i is the closure phase in a triangle at an observation time t_i, and σ_i denotes the uncertainty in ϕ_i. Note that we have assumed here Gaussian statistics for the measurements of closure phases. This assumption is not expected to introduce any significant changes in our quantitative results since the triangles we will be applying this method to are characterized by high signal-to-noise measurements. Applying this mixture model to data with large errors would require using an appropriate distribution for the closure-phase errors and their correlations (see Christian & Psaltis 2020).

The likelihood that n closure-phase observations in a given triangle across all four days of observation follow the model $\phi_{\text{model}}(t)$ is

$$L(c_0, c_1, c_2, \sigma_{c_0}) = \prod_{i=1}^{n} L_i(c_0, c_1, c_2, \sigma_{c_0}) \qquad (6)$$

$$= \prod_{i=1}^{n} \left\{ \frac{1}{\sqrt{2\pi(\sigma_i^2 + \sigma_{c_0}^2)}} \right\} \exp\left[-\sum_{i=1}^{n} \frac{1}{2} \frac{\{\phi_i - \phi_{\text{model}}(t_i)\}^2}{(\sigma_i^2 + \sigma_{c_0}^2)} \right]. \qquad (7)$$

Assuming flat priors in the polynomial coefficients and in σ_{c_0}, we map the parameter space using the Markov-chain Monte Carlo sampling.

Figure 3 shows the posteriors over two of the model parameters, c_0 and σ_{c_0}, for each of the three triangles that exhibits low day-to-day variability. The left panels show the 68% and 95% contours of the posteriors; the right panels show the data-driven model with the most likely value of the parameters, overplotted on the closure-phase observations in these triangles. The most likely standard deviations of variability across the six days of observations are $\sim 3°$–$5°$. This is comparable to the systematic error in closure-phase observations of $2°$ as reported in EHT Collaboration et al. (2019c) and is remarkably small.

3. GRMHD Simulations and Library

A large suite of GRMHD simulations has been generated to model the accretion flow around M87. The simulations have been performed using the algorithms harm (see Gammie et al. 2003), BHAC (Olivares Sánchez et al. 2018), KORAL (Sądowski et al. 2014), etc. The simulations have been initialized with two magnetic field configurations that led to different field structures in the flows: Standard and Normal Evolution (SANE; see Igumenshchev et al. 2003) and Magnetically Arrested Disk (MAD; see Narayan et al. 2012 and Sądowski et al. 2013). A comprehensive comparison of the GRMHD algorithms is presented in Porth et al. (2019). The set of observables that results from these simulations has been obtained by general relativistic ray tracing and radiative transfer algorithms, such as GRay (Chan et al. 2013) and ipole (Mościbrodzka & Gammie 2018).

In this paper, we analyze the GRMHD simulations that were run using harm (see Gammie et al. 2003; Narayan et al. 2012). The simulations include SANE and MAD configurations of the magnetic fields and different black hole spins with corotating or counterrotating accretion disks. The flow properties, as calculated in the GRMHD simulations, scale with the mass of the black hole and, therefore, the latter does not enter the calculation. The dependence of the electron temperature on the local value of the plasma β parameter aims to capture the effects of sub-grid electron physics that are not resolved in the GRMHD simulations (see Chan et al. 2015). The accretion flows in the simulations are modeled as collisionless plasmas, where the ratio of ion temperature to electron temperature ($R \equiv T_i/T_e$) is given by

$$R = R_{\text{high}} \frac{\beta^2}{1 + \beta^2} + \frac{1}{1 + \beta^2}. \qquad (8)$$

Here, $\beta \equiv P_{\text{gas}}/P_{\text{mag}}$ is the ratio of gas pressure (P_{gas}) to the magnetic pressure (P_{mag}). This prescription aims to simulate the effects of sub-grid electron heating, using this simple, physics-motivated parametric form (Mościbrodzka et al. 2016; and EHT Collaboration et al. 2019e).

General relativistic ray tracing and radiative transfer is performed on the simulated system at the wavelength of 1.3 mm in order to generate the images of the black hole using the different snapshots of the simulations. For radiative transfer, the black hole mass (M_{BH}) and the overall electron number-density scale in the accretion disk (n_e) set a scale for the mass and the optical depth in the accretion disk, which determines the mass accretion rate and the flux of emission in the source. It follows from the scaling properties of the emissivity of the accretion disk at 1.3 mm and from the natural scaling of the GRMHD simulations (see Chan et al. 2015) that n_e and M_{BH} are degenerate quantities with the resulting images and, therefore, the various interferometric observables, depending only on the product $M_{\text{BH}}n_e^2$ (see a derivation and discussion in the Appendix).

We use two sets of GRMHD models for studying closure-phase variability:

(i) The first set of models (henceforth Set A) is aimed at understanding the dependence of the closure-phase variability on the properties of the accretion flow, i.e., MAD versus SANE magnetic field configuration, the plasma prescription, and the electron number-density scale (n_e). In particular, they include SANE and MAD models for a single spin, three different values of R_{high}, and five different values of n_e (defined at a fiducial mass of $M_{\text{BH}} = 6.5 \times 10^9 M_\odot$). For this value of the black hole mass, this range allows us to explore compact fluxes that are up to a factor of a few above and below the nominal value of 0.5 Jy. Each model is used to generate 1024 images with a time cadence of 10 GM/c^3, amounting to a total of $\sim 30,000$ images in this set. Ray tracing and radiative transfer calculations for this simulation set are carried out using GRay.

(ii) The second set of models (henceforth Set B) explores a comprehensive set of black hole spins and R_{high} of the accretion plasma, which are used in EHT Collaboration et al. (2019e) in the interpretation of the EHT observations. The electron number-density scale (n_e) in this simulation set is tuned a priori such that the total flux of radiation at 1.3 mm is equal to 0.5 Jy for a fiducial mass of $M_{\text{BH}} = 6.2 \times 10^9 M_\odot$. Each model in this simulation set is used to generate 600–1000 images at a time cadence of 5 GM/c^3, amounting to $\sim 50,000$ images in this set. Ray tracing and radiative transfer calculations for this simulation set are carried out using ipole.

The ray tracing and radiative transfer tracing calculations on the GRMHD simulations performed using ipole and GRay ignore the effects of finite light travel time. Bronzwaer et al. (2018) showed that the effect of the approximation on the lightcurve of flux density in a simulation is restricted to only a few percent. Depending upon the nature of the spatial

Table 2
GRMHD Simulation Model Parameters

Parameter[a]	Parameter Space	
	Set A	Set B
Model type	MAD, SANE	MAD, SANE
Black hole spin[b]	+0.9	0.0, ±0.5, ±0.94
Plasma R_{high}	1, 20, 80	1, 10, 20, 40, 80, 160
Electron number density (n_e)[c]	1,2.5,5,7.5,10 ($\times 10^5$ cm^{-3})	Tuned to constant flux
Time cadence	10 GM/c^3	5 GM/c^3

Notes.
[a] The u–v coordinates of the baselines are rotated to align the spin axis of the black hole at a position angle of 288° east of north.
[b] The positive spin models are ray traced at an inclination of 163° and negative spin models at 17° in Set A. Set B models are ray traced at an inclination of 17°.
[c] The electron number density is defined at a fiducial mass of $6.5 \times 10^9 M_\odot$ for Set A and $6.2 \times 10^9 M_\odot$ for Set B.

correlations in structural variability in the simulation, the computed images may carry either time-correlated or time-uncorrelated features. These features will have an effect on the amplitude of variability inferred. In this study, we ignore these effects in inferring the variability in the images.

The parameter spaces studied in sets A and B are listed in Table 2. Although the mass of the black hole M_{BH} does not enter as an independent parameter in the calculation of the black hole images, it affects our interpretation of the observations in the following ways:

(i) The characteristic time unit (τ) in the GRMHD simulations is set by the mass of the black hole as $\tau = GM_{BH}/c^3$. A higher mass of the black hole implies that an observation span of 6 days would translate to a shorter elapsed time in units of τ.

(ii) The angular size of the image as seen by a distant observer depends on the black hole mass ($\Delta\theta \sim \lambda/M_{BH}$), which implies that the EHT probes different regions in the Fourier space for black holes of different masses. A higher mass of the black hole translates to the EHT probing structures at smaller length scales.

The mass of M87 has been measured using two methods prior to the EHT observations (EHT Collaboration et al. 2019e). Gebhardt et al. (2011) measured a mass of $M_{BH} = 6.6 \pm 0.4 \times 10^9 M_\odot$ using stellar dynamics. Walsh et al. (2013) measured a mass of $M_{BH} = 3.5^{+0.9}_{-0.7} \times 10^9 M_\odot$ by studying emission lines from ionized gas. The GRMHD models in simulation sets A and B give images for which the ring sizes and widths correspond to masses in the range inferred by the stellar dynamics measurement of Gebhardt et al. (2011; see EHT Collaboration et al. 2019f). Because of this, we allow the black hole mass to vary in the range $5 \times 10^9 M_\odot \leqslant M_{BH} \leqslant 9.5 \times 10^9 M_\odot$ in both sets of the simulations.

The orientation of the black hole spin axis has been constrained by long-wavelength observations of its jet at a position angle of ∼288° north of east and at an inclination of 17° with respect to the line of sight (see discussion in EHT Collaboration et al. 2019f). We trace the Set A models at an inclination of 17°. In Set B, we trace the positive spin models at an inclination of 163° and the negative spin models at 17°.

The simulations typically run for lengths that correspond to ∼ $10^4 GM/c^3$. Here, we only use images obtained from the relaxed turbulent state with a slowly varying mass accretion rate. This corresponds to simulation times in the range of $5 \times 10^3 \leqslant t \leqslant 10^4 GM/c^3$.

4. Closure-phase Variability in GRMHD Simulations

In order to analyze visibility phase and closure-phase variability in GRMHD models, we first transform the GRMHD snapshots into the visibility space by performing a two-dimensional Fourier transform on each of the images. We then compute the amplitude and phase from the complex visibilities at each location in the u–v plane.

Since the visibility phase is a directional quantity, we need to employ directional statistics to infer the standard deviation in a time-series. For a given time-series of n phases θ_i, we compute its directional dispersion as

$$D = \frac{1}{n}\sum_{i=1}^{n}\{1 - \cos(\theta_i - \bar{\theta})\}, \quad (9)$$

where $\bar{\theta}$ represents the circular mean, defined as

$$\bar{\theta} = \tan^{-1}\left\{\frac{\sum_{i=1}^{n}\sin(\theta_i)}{\sum_{i=1}^{n}\cos(\theta_i)}\right\}. \quad (10)$$

In the limit of small deviations in the time-series from the circular mean $\bar{\theta}$, the directional dispersion can be approximated as

$$D \approx \frac{\sigma^2}{2}, \quad (11)$$

where σ is inferred as a standard deviation of the time-series θ_i for small fluctuations about $\bar{\theta}$.

We use this quantity to construct heat maps of phase variability in order to understand the dependence of variability on the u–v coordinates (see also Medeiros et al. 2017). We present an example of such a heat map for one of the simulations in Set B in Figure 4. The left panel shows the mean visibility amplitude on the u–v plane computed across the simulation run and reveals deep visibility minima that are aligned with the spin axis of the black hole. The right panel shows a heat map of the visibility phase dispersion. There are *hot regions* of visibility phase variability, i.e., localized regions in u–v space that show large dispersions. These regions lie primarily along the spin axis of the black hole and at baseline lengths that correspond to the deep minima in visibility amplitudes. In fact, a natural anticorrelation between phase variability and mean visibility amplitude is observed in all the GRMHD models, which was also explored in Medeiros et al. (2017; see their Figures 3 and 4).

Based on this understanding, one expects the closure-phase variability computed along various triangles to depend on the locations of the three vertices in the u–v space. In particular, the localized nature of variability implies that closure triangles that have baselines crossing the hot regions are expected to exhibit high variability in closure phases, whereas triangles with vertices in quiet parts of the u–v space should show a low level of variability. In Figure 4, we show examples of two such triangles: the ALMA-SMA-LMT triangle has a baseline on a hot region and is expected to be highly variable, while a low-variability closure triangle (ALMA-LMT-SMT) avoids the hot regions.

The azimuthal extent of the hot regions of phase dispersion in the u–v plane depends on the degree of symmetry of the
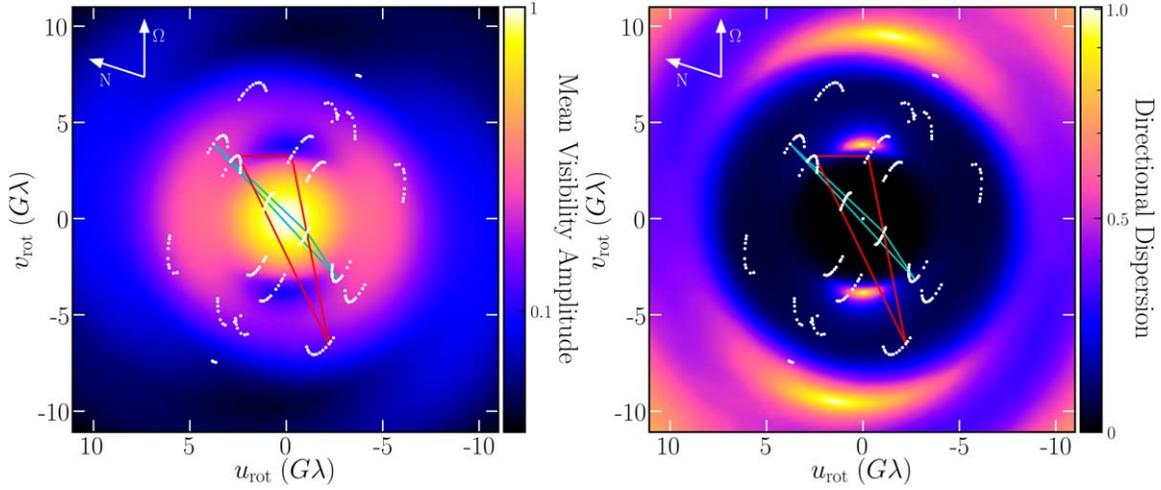
Figure 4. Normalized mean visibility amplitude map on a logarithmic scale (left) and directional dispersion map (see Equation (9)) of visibility phases (right) for the SANE, $a = +0.5$, $R_{high} = 1$ model from simulation set B. The black hole spin points upwards as indicated by the white arrow labeled as Ω. The EHT baseline coverage (on April 11) are shown by the white dots, and are rotated such that the spin points to a position angle of 288° east of north (with north indicated by the white arrow labeled by N and the u_{rot}–v_{rot} plane representing the rotated u–v plane). The cyan and the red triangles indicate the ALMA-LMT-SMT (at UTC 3:32:5.0003 hr/GMST 16:26:37.1531 hr) and ALMA-SMA-LMT (at UTC 5:00:5.0001 hr/GMST 17:54:51.6089 hr) triangles respectively. The second triangle includes the SMA-LMT baseline that crosses a visibility minimum, which translates to a high level of variability in the closure phase introduced by structural changes in the image. The mass of the black hole is set to $M_{BH} = 7.5 \times 10^9 M_\odot$.

underlying image. This is shown in Figure 7, where each column corresponds to a simulation from Set A with a different electron-density scale n_e, and all other black hole and plasma parameters held fixed. Qualitatively, the two effects of increasing the electron-density scale are a higher level of symmetry in the bright emission ring and an increase in its fractional width. The more symmetric images lead to a larger azimuthal extent in the minima in the visibility amplitudes (middle panels) and in the hot regions of phase dispersion (lower panels). The increased fractional width of the images lead to the locations of both the visibility amplitude minima and the hot regions in phase dispersion to appear at smaller baseline lengths.

4.1. Closure-phase Variability and Compliance Fractions

The phase dispersions discussed in the previous section were calculated across the entire span of the simulations, which corresponds to many dynamical timescales. In order to compare the simulations to the observed variability in M87, however, we need to calculate the degree of variability for a time span of $\Delta t = 6$ days, which is the longest separation between the four observations in 2017. Furthermore, because observations only yield closure phases, hereafter we focus on this quantity to facilitate comparisons.

We define the variance in closure phase $\phi_{cp}(t)$ for a time span of $\Delta t = 6$ days using Equation (11) as

$$\sigma^2(t_0) = \frac{1}{\Delta t} \int_{t_0}^{t_0 + \Delta t} dt \, 2[1 - \cos\{\phi_{cp}(t) - \bar{\phi}_{cp}\}]. \quad (12)$$

In order to reduce the discretization noise when calculating this quantity, we perform a linear interpolation between simulation time-steps and construct a continuous function $\phi_{cp}(t)$ representing the evolution of closure phases. We use fixed u–v locations taken at a median time over the night of observations, in order to construct this function. This ensures that we separate the evolution of closure phases due to the changing locations of the baselines from the structural variability of the images that we are interested in inferring.
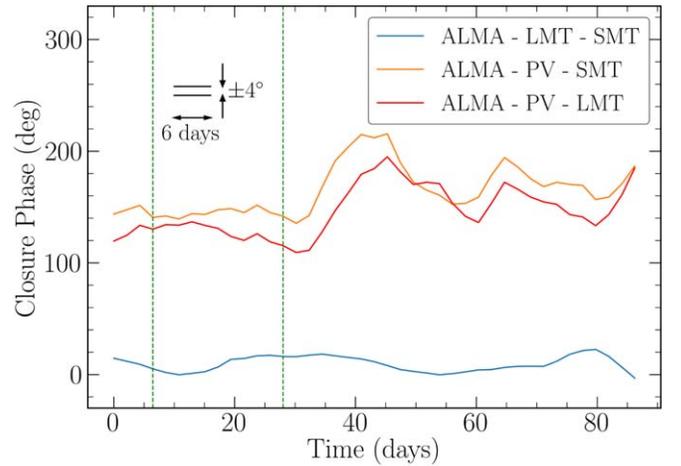
Figure 5. Closure phases for three triangles plotted as a function of time for a particular segment of the same simulation (Set B—MAD $a = +0.94$, $R_{high} = 20$). The black parallel lines indicate the timescale of 6 days and a standard deviation of ~4°. The section within the green dashed vertical lines indicates a region of low variability, and hence counts toward the compliance fraction of the model.

In Figure 5, we show the evolution of the closure phase with time during one segment of a simulation chosen from Set B, which has a MAD configuration with parameters $a = +0.94$ and $R_{high} = 20$. As is evident from this evolution, there are time spans where the closure phase shows little variability (e.g., the times between the green vertical lines) and others where there are substantial swings of order π over a short period of time that are comparable to the length of the observations. Given the low degree of variability observed for some triangles in M87 data (see Section 2), this motivates us to define a metric that quantifies how common such periods are in a given model.

Figure 6 shows the standard deviation in closure-phase variability computed from all 6 day segments in the simulation shown in Figure 5, for the three triangles that have observationally shown a small degree of variability. The dashed lines correspond to thresholds σ_1, σ_2, σ_3 of this
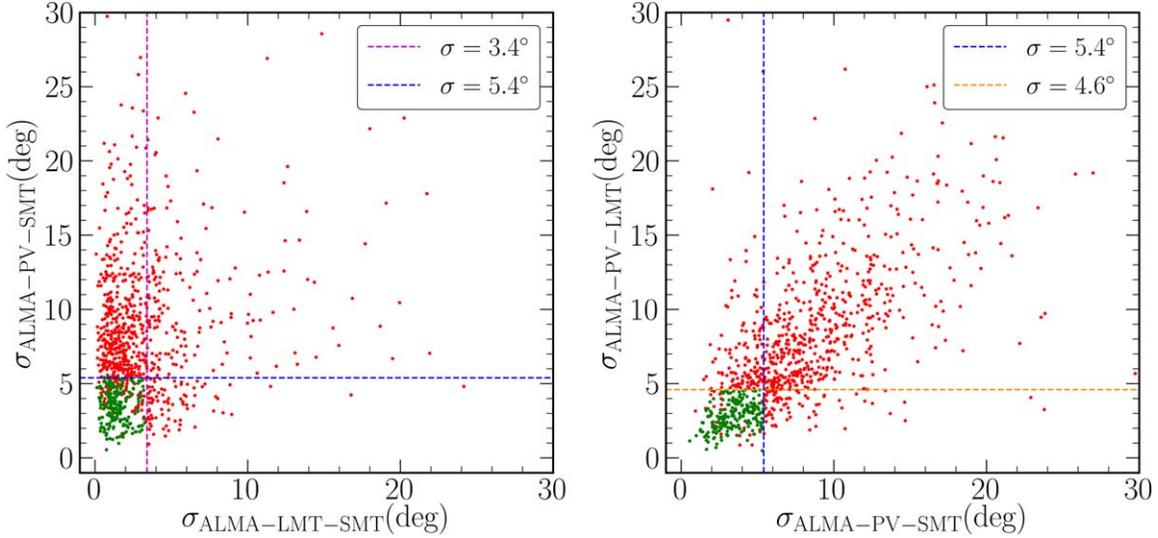
Figure 6. Two-dimensional scatter plots of inferred standard deviation in closure phases in three triangles across one simulation (simulation set B–MAD $a = +0.94$, $R_{high} = 20$). The horizontal and vertical dashed lines indicate the observational bounds for the standard deviation for each triangle, as described in Section 2.

Table 3
Compliance Fraction for Set A

Model	n_e ($\times 10^5 \mathrm{cm}^{-3}$)	R_{high}		
		1	20	80
SANE $a = +0.9$	1	41%	30%	24%
	2.5	37%	31%	24%
	5	31%	28%	25%
	7.5	24%	24%	22%
	10	18%	18%	20%
MAD $a = +0.9$	1	52%	36%	22%
	2.5	50%	32%	23%
	5	40%	22%	20%
	7.5	24%	15%	18%
	10	12%	12%	18%

observed variability. In Figure 5, we choose as the most likely values of σ_{c_0} in the corresponding triangles as the thresholds (see Table 1). The green points indicate the occurrences of 6 day segments that are consistent with observations. We define the quantity $\mathscr{F}(\sigma_1, \sigma_2, \sigma_3)$ of a model as the fraction of 6 day segments that shows a level of variability consistent with the observed one; i.e., the ratio of green points to the total number of points in this figure.

Formally, $\mathscr{F}(\sigma_1, \sigma_2, \sigma_3)$ can be written as

$$\mathscr{F}(\sigma_1, \sigma_2, \sigma_3) = \int_0^\infty d\sigma_1' \int_0^\infty d\sigma_2' \int_0^\infty d\sigma_3' \, P(\sigma_{sys})$$
$$\times P_{model}(\sigma_1', \sigma_2', \sigma_3' | \sigma_{sys}), \qquad (13)$$

where $P(\sigma_{sys})$ is the prior in the systematic uncertainty σ_{sys}, and $P_{model}(\sigma_1', \sigma_2', \sigma_3' | \sigma_{sys})$ is the three-dimensional distribution of circular standard deviations $\sigma_1', \sigma_2', \sigma_3'$ computed in the three low-variability triangles using Equation (12). The observed variability, as quantified in Section 2, is a combination of the true intrinsic variability of the source and the systematic errors in the measurement. Because of our limited knowledge of the systematic uncertainties and their priors, we assume a form

such that Equation (13) can be written as

$$\mathscr{F}(\sigma_1, \sigma_2, \sigma_3) = \int_0^{\sigma_1} d\sigma_1' \int_0^{\sigma_2} d\sigma_2'$$
$$\times \int_0^{\sigma_3} d\sigma_3' \, P_{model}(\sigma_1', \sigma_2', \sigma_3'), \qquad (14)$$

i.e., simply assuming that the combined intrinsic degree of variability and the systematic uncertainties cannot exceed the inferred values.

Because our inferred degree of variability from the observations themselves have associated formal errors as described by the marginalized posteriors $P(\sigma_1)$, $P(\sigma_2)$, and $P(\sigma_3)$ as shown in Figure 3; we compute the compliance fraction by integrating over those posteriors using

$$\mathscr{C}(model) = \int d\sigma_1 d\sigma_2 d\sigma_3 P(\sigma_1) P(\sigma_2) P(\sigma_3) \mathscr{F}(\sigma_1, \sigma_2, \sigma_3).$$
$$(15)$$

The compliance fraction denotes the expectation value of $\mathscr{F}(\sigma_1, \sigma_2, \sigma_3)$ given the probability distributions of σ_1, σ_2, and σ_3.

We compute this compliance fraction for black hole masses in the range $5 \times 10^9 M_\odot \leqslant M_{BH} \leqslant 9.5 \times 10^9 M_\odot$ and use the maximum number as the compliance fraction for a given GRMHD model.

5. Comparison of GRMHD Simulations to M87 Observations

In this section, we use the two sets of simulations we discuss in Section 3 to explore the dependence of the compliance fraction on the magnetic field configuration, electron temperature prescription in the plasma, and electron-density scale (Set A), as well as on the black hole spin (Set B). These two sets are meant to serve as two slices in the large parameter space of simulations.

Table 3 shows the compliance fractions calculated for the 30 simulations in Set A. Overall, these compliance fractions are rather small, indicating that a lot of simulations show more frequent periods of high variability, even in the triangles that observationally do not exhibit large changes in the closure
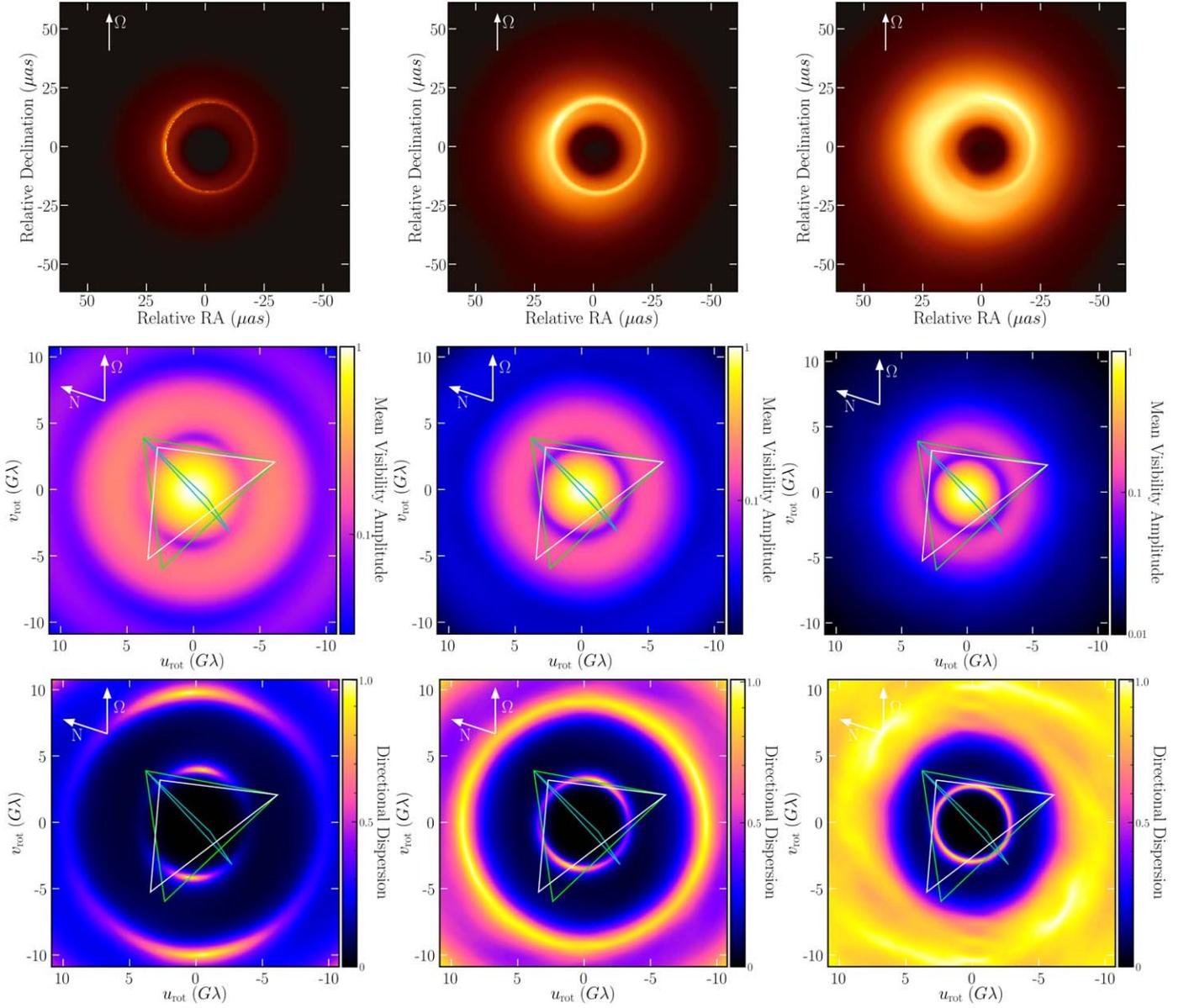
Figure 7. The average images (top), normalized average visibility amplitudes (middle), and directional phase dispersion (bottom) of the MAD, a = 0.9, $R_{high} = 20$ simulation. Models with three electron number densities—$n_e = 1 \times 10^5$ cm^{-3} (left), $n_e = 5 \times 10^5$ cm^{-3} (middle), and $n_e = 1 \times 10^6$ cm^{-3} (right), are mapped in this figure. The white arrows labeled as Ω indicate the spin vector of the black hole, and the ones labeled as N indicate the north direction. The coordinates (u_{rot}, v_{rot}) represent the u–v coordinates rotated such that the spin points to a position angle of 288° east of north. It is evident that a model with lower n_e exhibits an emission dominant from the photon ring, and has a lower variability in visibility phases outside the first visibility minimum. The three triangles plane indicate the low-variability triangles—ALMA-LMT-SMT (cyan), ALMA-PV-SMT (green), and ALMA-PV-LMT (white) at UTC 3:32:5.0003 hr/ GMST 16:26:37.1531 hr. The colormap in the visibility amplitude is in logarithmic scale with the maximum value normalized to unity.

phase across the six days of the campaign. The dominant distinguishing characteristic of the simulations that show a higher compliance fraction is the small value for the electron-density scale. There is a smaller difference in compliance fractions between the MAD and SANE simulations. We observe that, for small values of R_{high}, the dependence of the compliance fraction on the fractional width is stronger.

We explored how the electron-density scale affects the image structure and variability. To this end, we calculated the characteristic properties of the average image in each simulation, using the image-domain techniques discussed in EHT Collaboration et al. (2019d, 2019f). We measured the fractional width of each average image δw_f as the ratio of the width δw to the ring diameter d, i.e., $\delta w_f \equiv \delta w/d$. We found the

fractional widths of the images correlate strongly with the electron-density scale, as shown in Figure 8. This is expected, given that increasing the electron-density scale also increases the emissivity and optical depth in the accretion flow, as shown in the top panels of Figure 7 (Chan et al. 2015).

The right panel of Figure 8 shows, indeed, that the compliance fraction is anticorrelated with the fractional width of the average images of the simulations. When the bright emission ring in an image is narrow, it traces the outline of the black hole shadow and, therefore, its shape and brightness distribution is determined primarily by gravitational lensing effects. On the other hand, when the bright emission ring is broad, variability due to the turbulence in the accretion flow introduces more apparent effects. The low level of variability
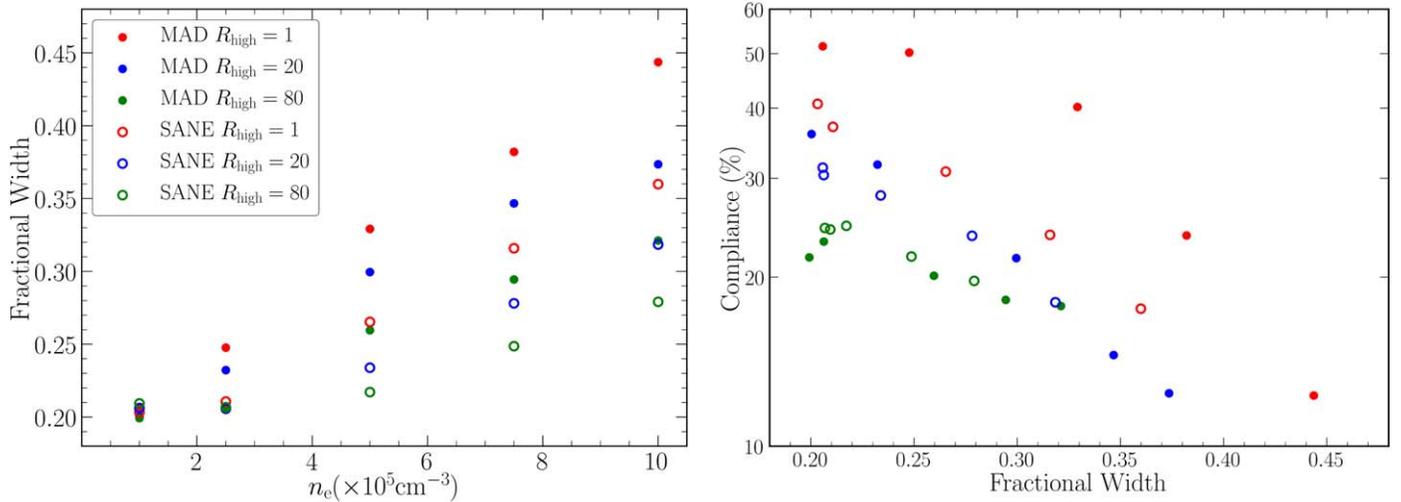
Figure 8. Left: the fractional width of the ring of emission in the average image of each simulation in Set A. Right: the anticorrelation between the fractional width and compliance fraction in the simulation set A.

Table 4
Compliance Fraction for Set B

Model	Spin	R_{high}					
		1	10	20	40	80	160
SANE	−0.94	<1% [a,b,c]	2% [a,b,c]	3% [a,b,c]	2% [a,b,c]	1% [a,b,c]	<1% [a,b,c]
	−0.5	<1% [a]	12% [a]	12% [a,b]	12% [a,b]	8% [a,b]	7% [a,b]
	0.0	<1% [a,b]	3% [a,b]	8% [a]	11% [a,b]	11% [a,b]	10% [a,b]
	+0.5	6% [a,b]	2% [a,b]	2% [a,b]	6% [a,b]	10% [a,b]	10% [a,b]
	+0.94	21% [b]	21% [b]	15% [a,b]	15% [a,b]	19% [a,b,c]	24% [a,b,c]
MAD	−0.94	7% [b,c]	6% [a,b,c]	7% [a,b,c]	6% [a,b,c]	6% [a,b,c]	9% [a,b,c]
	−0.5	10% [b]	12% [a,b]	13% [a,b,c]	11% [a,b,c]	11% [a,b,c]	11% [a,b,c]
	0.0	12% [b]	11% [a,b]	15% [a,b]	13% [a,b]	10% [a,b]	9% [a,b]
	+0.5	11% [b]	16% [a,b,c]	18% [a,b,c]	19% [a,b,c]	18% [a,b,c]	17% [a,b,c]
	+0.94	20% [c]	24% [b,c]	24% [a,b,c]	20% [a,b,c]	16% [a,b,c]	12% [a,b,c]

Notes.
[a] Satisfies radiative efficiency constraint.
[b] Satisfies X-ray luminosity constraint.
[c] Satisfies jet power constraint.

across the six days observed in M87 argues in favor of images characterized by thin (∼20%) rings of emission.

In the simulations of Set B, the electron number-density scale was tuned to generate a fixed source flux of 0.5 Jy. Different configurations were explored with both rotating and counterrotating black hole spins of various magnitudes. The compliance fractions are shown in Table 4 and are, overall, lower than those of the Set A simulations. As in the previous case, the MAD simulations have on average a higher compliance fraction than the SANE simulations, and there is only a marginal dependence on the electron temperature parameter R_{high}. However, there is a significant dependence on the spin of the black hole, with corotating, high-spin simulations producing the highest compliance fractions.

The table also shows constraints imposed on the models of Set B by other considerations, not originating from the EHT observations (EHT Collaboration et al. 2019e). They include constraints related to (a) the simulations having achieved radiative equilibrium, (b) the predicted X-Ray flux to be $L_X = (4.4 \pm 0.1) \times 10^{40}$ erg s^{-1}, as measured during the nearly simultaneous observations with the Chandra X-Ray

Observatory and the Nuclear Spectroscopic Telescope Array (NuSTAR), and (c) the jet power being in range 10^{42} to 10^{45} erg s^{-1}. Simulations with fast black hole spins, which are consistent with these constraints, are also characterized by larger compliance fractions, giving preference to these models.

6. Discussion

In this paper, we studied the variability of the black hole image structure of M87 at timescales comparable to the fastest dynamical timescale near the horizon, as it is imprinted on the closure phases measured during the EHT 2017 observations. We identified three linearly independent closure triangles that exhibit a persistent evolution pattern of closure phases over the course of each night of observation but show little variation around this pattern across the six days of observations, namely, ALMA-LMT-SMT, ALMA-PV-SMT, and ALMA-PV-LMT. In other words, the closure-phase evolution in these triangles follows set tracks determined by the rotation of the baselines on the u–v plane but shows very little scatter around these tracks from day to day. We quantified the degree of variability in these triangles to be ∼3°–5°. This inferred level of variability is

comparable to the $\sim 2°$ systematic error in measurement of closure phases (EHT Collaboration et al. 2019c).

We also found three triangles that exhibit a high level of day-to-day variability, namely, ALMA-SMA-LMT, ALMA-SMA-SMT, and ALMA-PV-SMA. The change in the closure phase across 6 days in a given location on the u–v plane for these triangles can be $\sim 90°$–$180°$. We identified them as triangles with at least one baseline that encounters a deep visibility minimum on the u–v plane. This is in agreement with expectations based on theoretical models that reveal the presence of highly variable but highly localized regions on the u–v plane associated with the locations of these minima.

We used GRMHD simulations to explore the dependence of closure-phase variability on different model parameters and at different locations in the u–v plane. We found that the most discriminating image characteristic of models in terms of the degree of closure-phase variability is the fractional width of the ring of high intensity on the image. Models that best reproduce the observed small level of variability are those with thin ring-like images with structures dominated by gravitational lensing effects and thus least affected by turbulence in the accreting plasmas.

Among the models we explored, there is marginal difference between SANE and MAD simulations, which explore different magnetic field configurations in the accretion flows, with some preference for the MAD models. There is also a small dependence on the black hole spin, with the high-spin corotating models showing the lowest level of day-to-day variability, in agreement with the observations.

These findings demonstrate that the method we introduced to quantify the day-to-day variability in the closure-phase data and compare it to the models is a useful tool in exploring the origin of variability in horizon-scale images of black holes and in discriminating between models.

Appendix
Approximate Degeneracy of the Radiative Transfer Solution

In this appendix, we present analytical arguments to show that the mm-wavelength images calculated from GRMHD simulations of accretion flows with parameters relevant to the M87 black hole are approximately invariant to the product $n_e^2 M_{BH}$, where n_e is the electron-density scale and M_{BH} is the mass of the black hole.

The radiative transfer equation at a frequency ν is given by

$$\frac{dI_\nu}{ds} = \eta_\nu - \chi_\nu I_\nu, \qquad (A1)$$

where I_ν denotes the specific intensity at a frequency ν, s denotes the distance traveled along the path of a photon, η_ν denotes the emissivity of the medium, and χ_ν denotes the opacity of the medium. Equation (A1) can be recast as

$$\frac{dI_\nu}{ds} = \chi_\nu \left(\frac{\eta_\nu}{\chi_\nu} - I_\nu \right). \qquad (A2)$$

The fraction η_ν/χ_ν is the source function S_ν and, for thermal emission, is equal to the blackbody function, which depends solely on temperature T. We denote this as $\eta_\nu/\chi_\nu \equiv \mathscr{B}_\nu(T)$.

Throughout this work, we use the analytic approximation devised by Leung et al. (2011) for synchrotron emissivity from a thermal distribution of relativistic electrons

$$\eta_\nu = n_e \frac{\sqrt{2}\,\pi e^2 \nu_s}{3K_2(1/\Theta_e)c}(X^{1/2} + 2^{11/12}X^{1/6})^2 \exp(-X^{1/3}), \quad \text{(A3)}$$

where $X \equiv \nu/\nu_s$, $\nu_s \equiv (2/9)\nu_c\Theta_e^2\sin\theta$, $\nu_c \equiv eB/(2\pi m_e c)$, $\Theta_e \equiv k_b T_e/(m_e c^2)$ is the dimensionless electron temperature, and K_2 denotes the modified Bessel function of the second kind. In the these expressions, θ denotes the angle between the magnetic field and the emitted photon, B denotes the magnetic field strength, and T_e denotes the electron temperature. We use the constants m_e, e, k_b, and c to denote the electron mass, electron charge, the Boltzmann's constant, and the speed of light respectively. It is explicit in this expression that the synchrotron emissivity and opacity, for a given electron temperature and magnetic field, scale proportionally to the electron number density n_e. We show here that, for the parameters of the black hole at the center of the M87 galaxy, the synchrotron opacity and emissivity at a wavelength of $\lambda = 1.3$ mm also scale proportionally to a power of the magnetic field, i.e., $\propto B^\alpha$, with $\alpha \sim 2$.

We estimate the properties of the plasma in the inner accretion flow of M87 using the following analytic model. The electron density at a given radius r is given by the continuity equation, assuming a spherical accretion rate $\dot{M}$ via the relation

$$\dot{M} = 4\pi r^2 \left(\frac{h}{r}\right)m_p n_e u^r, \quad \text{(A4)}$$

where h/r is the scale height of the accretion flow, m_p is the proton mass (assuming fully ionized hydrogen), and u^r is the radial component of the accretion flow. We take the latter to be a fraction ξ of the freefall velocity, i.e.,

$$u^r = \xi\left(\frac{GM_{BH}}{r}\right)^{1/2}. \quad \text{(A5)}$$

We also express the accretion rate as $\dot{M} \equiv \dot{m}\dot{M}_E$, in terms of the Eddington accretion rate defined by

$$\dot{M}_E \equiv \frac{L_E}{\epsilon c^2} = \frac{4\pi GM_{BH}m_p}{\epsilon c\sigma_T}, \quad \text{(A6)}$$

where L_E is the Eddington critical luminosity, ϵ is the radiative efficiency of the flow, σ_T is the Thomson cross section, and $\dot{m}$ is the mass accretion rate in units of the Eddington accretion rate. Under these conditions, the electron density is

$$n_e = \left(\frac{c^2}{GM_{BH}\sigma_T}\right)\dot{m}\epsilon^{-1}\xi^{-1}\left(\frac{h}{r}\right)^{-1}\left(\frac{rc^2}{GM_{BH}}\right)^{-3/2}$$
$$= 7 \times 10^5 \left(\frac{M_{BH}}{6.5 \times 10^9 M_\odot}\right)^{-1}\left(\frac{\dot{m}}{2 \times 10^{-5}}\right)$$
$$\left(\frac{rc^2}{5GM_{BH}}\right)^{-3/2} \text{cm}^{-3}, \quad \text{(A7)}$$

where in the last expression we have used typical values for the M87 black hole and set $\xi = \epsilon = 0.1$ and $h/r = 0.4$.

Because of the radiatively inefficient character of the accretion flow around the M87 black hole, the ion temperature T_i is a fraction of the virial temperature

$$T_v = \frac{GM_{BH}m_p}{3k_B r}. \quad \text{(A8)}$$

It is also customary to write the electron temperature as a fraction $1/R$ of the ion temperature, i.e.,

$$T_e = \frac{1}{R}\left(\frac{GM_{BH}m_p}{3k_B r}\right)\left(\frac{T_i}{T_v}\right). \quad \text{(A9)}$$

Finally, we write the magnetic field in terms of the plasma β parameter as

$$n_e k_B(T_i + T_e) = \beta\frac{B^2}{8\pi} \quad \text{(A10)}$$

such that

$$B = 2c^2\left(\frac{2\pi m_p}{3GM_{BH}\sigma_T}\right)^{1/2}\left[\frac{\dot{m}(1 + R)}{\epsilon\xi\beta R}\right]^{1/2}$$
$$\times \left(\frac{T_i}{T_v}\right)^{1/2}\left(\frac{h}{r}\right)^{-1/2}\left(\frac{rc^2}{GM_{BH}}\right)^{-5/4}$$
$$= 9\left(\frac{M_{BH}}{6.5 \times 10^9 M_\odot}\right)^{-1/2}\left(\frac{\dot{m}}{2 \times 10^{-5}}\right)^{1/2}\left(\frac{rc^2}{5GM_{BH}}\right)^{-5/4} \text{G}, \quad \text{(A11)}$$

and we have set $T_i/T_v = 1/3$ and $\beta = 10$.

Figure 9 shows the ratio η_ν/n_e evaluated at the observed frequency of the EHT ($\nu = 230$ GHz, $\lambda = 1.33$ mm) and at a radial distance $r = 5GM_{BH}/c^2$, as a function of the strength of the magnetic field B, for the values of the various parameters used in the previous equations, i.e., for the conditions of the inner accretion flow around the black hole at the center of M87. This figure demonstrates that, over a broad range of magnetic field strengths (spanning more than an order of magnitude), the synchrotron emissivity scales approximately as $\eta_\nu \sim n_e B^\alpha$, with $\alpha \simeq 2$. This allows us to write the emissivity as

$$\eta_\nu \simeq n_e B^\alpha \mathcal{B}_\nu(T)f_\nu(T, \boldsymbol{r}), \quad \text{(A12)}$$

and the opacity as

$$\chi_\nu \simeq n_e B^\alpha f_\nu(T, \boldsymbol{r}), \quad \text{(A13)}$$

where $f_\nu(T, \boldsymbol{r})$ captures the scaling of the opacity with temperature T and the location in the accretion flow (see similar arguments in Chan et al. 2015).

In order to calculate the various simulated images, we used the plasma properties from long GRMHD simulations. Nonradiative GRMHD simulations are invariant to a rescaling of the density by a factor $\mathcal{M}$, as long as the magnetic field is also rescaled by a factor of $\mathcal{M}^{1/2}$ and the internal energy by a factor of $\mathcal{M}$. In other words, $B \sim n_e^{1/2}$ and the Alfvén speed $B/(m_p n_e)^{1/2}$ are the quantity that remains invariant under rescaling. Combined with the approximate expressions (A12)–(A13) derived above, this implies that the synchrotron emissivity and opacity evaluated using the simulation outputs are invariant to rescaling, as long as the product $n_e B^\alpha \sim n_e^{1+\alpha/2}$ remains constant.

Finally, the integration of the transfer equation is performed on a coordinate system in which the distances are expressed in
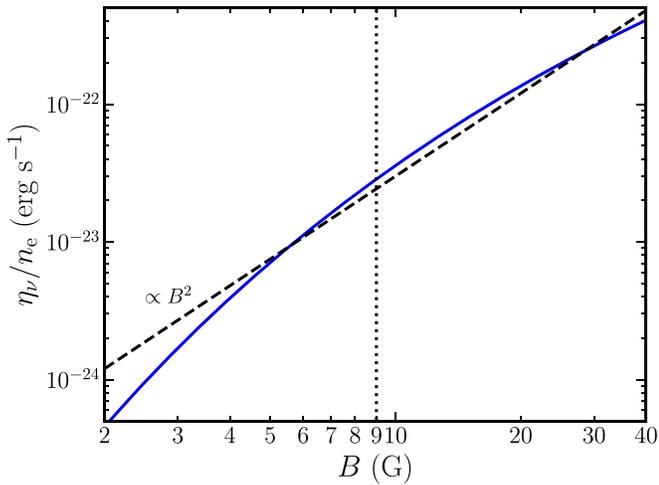
Figure 9. The ratio of the thermal synchrotron emissivity η_ν to the electron density n_e, as a function of the strength of the magnetic field, evaluated at an observing frequency of the EHT, $\nu = 230$ GHz, and for parameters appropriate to the inner accretion flow in the black hole at the center of the M87 galaxy (see text). The vertical dashed line shows the inferred strength of the magnetic field near the black hole horizon. The dashed line shows the approximate $\sim B^2$ scaling.

terms of the length scale set by the mass of the black hole, i.e.,

$$ds \equiv ds'\left(\frac{GM_{\mathrm{BH}}}{c^2}\right). \tag{A14}$$

Rewriting Equation (A2) using the scaling (A12)–(A14), we find

$$\frac{dI}{ds'} = n_{\mathrm{e}}^{1+\alpha/2} f(T, \boldsymbol{r}) \frac{GM_{\mathrm{BH}}}{c^2}[\mathscr{B}(T) - I] \tag{A15}$$

$$= (n_{\mathrm{e}}^{1+\alpha/2} M_{\mathrm{BH}}) \frac{G}{c^2} f(T, \boldsymbol{r})[\mathscr{B}(T) - I]. \tag{A16}$$

We drop the ν in subscript to indicate quantities calculated at $\nu = 230$ GHz. From this last expression, it is apparent that the electron number density n_{e} and the black hole mass M_{BH} are degenerate quantities in the solution of the radiative transfer problem at wavelengths where the dominant source of opacity is due to synchrotron processes, with a degeneracy in the product $n_{\mathrm{e}}^{1+\alpha/2} M_{\mathrm{BH}}$ and with $\alpha \simeq 2$.

ORCID iDs

Kaushik Satapathy ⓘ https://orcid.org/0000-0003-0433-3585
Lia Medeiros ⓘ https://orcid.org/0000-0003-2342-6728
Sean T. Dougall ⓘ https://orcid.org/0000-0002-3769-1314
Chi-Kwan Chan ⓘ https://orcid.org/0000-0001-6337-6126
Maciek Wielgus ⓘ https://orcid.org/0000-0002-8635-4242
George N. Wong ⓘ https://orcid.org/0000-0001-6952-2147
Charles F. Gammie ⓘ https://orcid.org/0000-0001-7451-8935
Kazunori Akiyama ⓘ https://orcid.org/0000-0002-9475-4254
Antxon Alberdi ⓘ https://orcid.org/0000-0002-9371-1033
Juan Carlos Algaba ⓘ https://orcid.org/0000-0001-6993-1696
Richard Anantua ⓘ https://orcid.org/0000-0003-3457-7660
Rebecca Azulay ⓘ https://orcid.org/0000-0002-2200-5393
Anne-Kathrin Baczko ⓘ https://orcid.org/0000-0003-3090-3975
Mislav Baloković ⓘ https://orcid.org/0000-0003-0476-6647
John Barrett ⓘ https://orcid.org/0000-0002-9290-0764

Bradford A. Benson ⓘ https://orcid.org/0000-0002-5108-6823
Lindy Blackburn ⓘ https://orcid.org/0000-0002-9030-642X
Raymond Blundell ⓘ https://orcid.org/0000-0002-5929-5857
Katherine L. Bouman ⓘ https://orcid.org/0000-0003-0077-4367
Geoffrey C. Bower ⓘ https://orcid.org/0000-0003-4056-9982
Hope Boyce ⓘ https://orcid.org/0000-0002-6530-5783
Christiaan D. Brinkerink ⓘ https://orcid.org/0000-0002-2322-0749
Roger Brissenden ⓘ https://orcid.org/0000-0002-2556-0894
Silke Britzen ⓘ https://orcid.org/0000-0001-9240-6734
Avery E. Broderick ⓘ https://orcid.org/0000-0002-3351-760X
Thomas Bronzwaer ⓘ https://orcid.org/0000-0003-1151-3971
Do-Young Byun ⓘ https://orcid.org/0000-0003-1157-4109
Andrew Chael ⓘ https://orcid.org/0000-0003-2966-6220
Koushik Chatterjee ⓘ https://orcid.org/0000-0002-2825-3590
Shami Chatterjee ⓘ https://orcid.org/0000-0002-2878-1502
Ilje Cho ⓘ https://orcid.org/0000-0001-6083-7521
Pierre Christian ⓘ https://orcid.org/0000-0001-6820-9941
John E. Conway ⓘ https://orcid.org/0000-0003-2448-9181
James M. Cordes ⓘ https://orcid.org/0000-0002-4049-1882
Thomas M. Crawford ⓘ https://orcid.org/0000-0001-9000-5013
Geoffrey B. Crew ⓘ https://orcid.org/0000-0002-2079-3189
Alejandro Cruz-Osorio ⓘ https://orcid.org/0000-0002-3945-6342
Yuzhu Cui ⓘ https://orcid.org/0000-0001-6311-4345
Jordy Davelaar ⓘ https://orcid.org/0000-0002-2685-2434
Mariafelicia De Laurentis ⓘ https://orcid.org/0000-0002-9945-682X
Roger Deane ⓘ https://orcid.org/0000-0003-1027-5043
Jessica Dempsey ⓘ https://orcid.org/0000-0003-1269-9667
Gregory Desvignes ⓘ https://orcid.org/0000-0003-3922-4055
Jason Dexter ⓘ https://orcid.org/0000-0003-3903-0373
Sheperd S. Doeleman ⓘ https://orcid.org/0000-0002-9031-0904
Ralph P. Eatough ⓘ https://orcid.org/0000-0001-6196-4135
Heino Falcke ⓘ https://orcid.org/0000-0002-2526-6724
Joseph Farah ⓘ https://orcid.org/0000-0003-4914-5625
Vincent L. Fish ⓘ https://orcid.org/0000-0002-7128-9345
Ed Fomalont ⓘ https://orcid.org/0000-0002-9036-2747
H. Alyson Ford ⓘ https://orcid.org/0000-0002-9797-0972
Raquel Fraga-Encinas ⓘ https://orcid.org/0000-0002-5222-1361
Per Friberg ⓘ https://orcid.org/0000-0002-8010-8454
Antonio Fuentes ⓘ https://orcid.org/0000-0002-8773-4933
Peter Galison ⓘ https://orcid.org/0000-0002-6429-3872
Roberto García ⓘ https://orcid.org/0000-0002-6584-7443
Boris Georgiev ⓘ https://orcid.org/0000-0002-3586-6424
Ciriaco Goddi ⓘ https://orcid.org/0000-0002-2542-7743
Roman Gold ⓘ https://orcid.org/0000-0003-2492-1966
Arturo I. Gómez-Ruiz ⓘ https://orcid.org/0000-0001-9395-1670
José L. Gómez ⓘ https://orcid.org/0000-0003-4190-7613
Minfeng Gu (顾敏峰) ⓘ https://orcid.org/0000-0002-4455-6946
Mark Gurwell ⓘ https://orcid.org/0000-0003-0685-3621
Kazuhiro Hada ⓘ https://orcid.org/0000-0001-6906-772X
Daryl Haggard ⓘ https://orcid.org/0000-0001-6803-2138
Ronald Hesper ⓘ https://orcid.org/0000-0003-1918-6098

Luis C. Ho (何子山) ● https://orcid.org/0000-0001-6947-5846

Mareki Honma ● https://orcid.org/0000-0003-4058-9000

Chih-Wei L. Huang ● https://orcid.org/0000-0001-5641-3953

Lei Huang (黄磊) ● https://orcid.org/0000-0002-1923-227X

Shiro Ikeda ● https://orcid.org/0000-0002-2462-1448

Sara Issaoun ● https://orcid.org/0000-0002-5297-921X

David J. James ● https://orcid.org/0000-0001-5160-4486

Michael Janssen ● https://orcid.org/0000-0001-8685-6544

Britton Jeter ● https://orcid.org/0000-0003-2847-1712

Wu Jiang (江悟) ● https://orcid.org/0000-0001-7369-3539

Michael D. Johnson ● https://orcid.org/0000-0002-4120-3029

Svetlana Jorstad ● https://orcid.org/0000-0001-6158-1708

Taehyun Jung ● https://orcid.org/0000-0001-7003-8643

Mansour Karami ● https://orcid.org/0000-0001-7387-9333

Tomohisa Kawashima ● https://orcid.org/0000-0001-8527-0496

Garrett K. Keating ● https://orcid.org/0000-0002-3490-146X

Mark Kettenis ● https://orcid.org/0000-0002-6156-5617

Dong-Jin Kim ● https://orcid.org/0000-0002-7038-2118

Jae-Young Kim ● https://orcid.org/0000-0001-8229-7183

Jongsoo Kim ● https://orcid.org/0000-0002-1229-0426

Junhan Kim ● https://orcid.org/0000-0002-4274-9373

Motoki Kino ● https://orcid.org/0000-0002-2709-7338

Jun Yi Koay ● https://orcid.org/0000-0002-7029-6658

Patrick M. Koch ● https://orcid.org/0000-0003-2777-5861

Shoko Koyama ● https://orcid.org/0000-0002-3723-3372

Carsten Kramer ● https://orcid.org/0000-0002-4908-4925

Michael Kramer ● https://orcid.org/0000-0002-4175-2271

Thomas P. Krichbaum ● https://orcid.org/0000-0002-4892-9586

Cheng-Yu Kuo ● https://orcid.org/0000-0001-6211-5581

Tod R. Lauer ● https://orcid.org/0000-0003-3234-7247

Sang-Sung Lee ● https://orcid.org/0000-0002-6269-594X

Aviad Levis ● https://orcid.org/0000-0001-7307-632X

Yan-Rong Li (李彦荣) ● https://orcid.org/0000-0001-5841-9179

Zhiyuan Li (李志远) ● https://orcid.org/0000-0003-0355-6437

Michael Lindqvist ● https://orcid.org/0000-0002-3669-0715

Rocco Lico ● https://orcid.org/0000-0001-7361-2460

Greg Lindahl ● https://orcid.org/0000-0002-6100-4772

Jun Liu (刘俊) ● https://orcid.org/0000-0002-7615-7499

Kuo Liu ● https://orcid.org/0000-0002-2953-7376

Elisabetta Liuzzo ● https://orcid.org/0000-0003-0995-5201

Laurent Loinard ● https://orcid.org/0000-0002-5635-3345

Ru-Sen Lu (路如森) ● https://orcid.org/0000-0002-7692-7967

Nicholas R. MacDonald ● https://orcid.org/0000-0002-6684-8691

Jirong Mao (毛基荣) ● https://orcid.org/0000-0002-7077-7195

Nicola Marchili ● https://orcid.org/0000-0002-5523-7588

Sera Markoff ● https://orcid.org/0000-0001-9564-0876

Daniel P. Marrone ● https://orcid.org/0000-0002-2367-1080

Alan P. Marscher ● https://orcid.org/0000-0001-7396-3332

Iván Martí-Vidal ● https://orcid.org/0000-0003-3708-9611

Satoki Matsushita ● https://orcid.org/0000-0002-2127-7880

Karl M. Menten ● https://orcid.org/0000-0001-6459-0669

Izumi Mizuno ● https://orcid.org/0000-0002-7210-6264

Yosuke Mizuno ● https://orcid.org/0000-0002-8131-6730

James M. Moran ● https://orcid.org/0000-0002-3882-4414

Kotaro Moriyama ● https://orcid.org/0000-0003-1364-3761

Monika Moscibrodzka ● https://orcid.org/0000-0002-4661-6332

Cornelia Müller ● https://orcid.org/0000-0002-2739-2994

Alejandro Mus Mejías ● https://orcid.org/0000-0003-0329-6874

Gibwa Musoke ● https://orcid.org/0000-0003-1984-189X

Hiroshi Nagai ● https://orcid.org/0000-0003-0292-3645

Neil M. Nagar ● https://orcid.org/0000-0001-6920-662X

Masanori Nakamura ● https://orcid.org/0000-0001-6081-2420

Ramesh Narayan ● https://orcid.org/0000-0002-1919-2730

Iniyan Natarajan ● https://orcid.org/0000-0001-8242-4373

Joey Neilsen ● https://orcid.org/0000-0002-8247-786X

Roberto Neri ● https://orcid.org/0000-0002-7176-4046

Chunchong Ni ● https://orcid.org/0000-0003-1361-5699

Aristeidis Noutsos ● https://orcid.org/0000-0002-4151-3860

Michael A. Nowak ● https://orcid.org/0000-0001-6923-1315

Héctor Olivares ● https://orcid.org/0000-0001-6833-7580

Gisela N. Ortiz-León ● https://orcid.org/0000-0002-2863-676X

Daniel C. M. Palumbo ● https://orcid.org/0000-0002-7179-3816

Jongho Park ● https://orcid.org/0000-0001-6558-9053

Ue-Li Pen ● https://orcid.org/0000-0003-2155-9578

Dominic W. Pesce ● https://orcid.org/0000-0002-5278-9221

Richard Plambeck ● https://orcid.org/0000-0001-6765-9609

Oliver Porth ● https://orcid.org/0000-0002-4584-2557

Felix M. Pötzl ● https://orcid.org/0000-0002-6579-8311

Jorge A. Preciado-López ● https://orcid.org/0000-0002-4146-0113

Hung-Yi Pu ● https://orcid.org/0000-0001-9270-8812

Venkatessh Ramakrishnan ● https://orcid.org/0000-0002-9248-086X

Ramprasad Rao ● https://orcid.org/0000-0002-1407-7944

Mark G. Rawlings ● https://orcid.org/0000-0002-6529-202X

Luciano Rezzolla ● https://orcid.org/0000-0002-1330-7103

Bart Ripperda ● https://orcid.org/0000-0002-7301-3908

Freek Roelofs ● https://orcid.org/0000-0001-5461-3687

Eduardo Ros ● https://orcid.org/0000-0001-9503-4892

Mel Rose ● https://orcid.org/0000-0002-2016-8746

Alan L. Roy ● https://orcid.org/0000-0002-1931-0135

Chet Ruszczyk ● https://orcid.org/0000-0001-7278-9707

Kazi L. J. Rygl ● https://orcid.org/0000-0003-4146-9043

David Sánchez-Arguelles ● https://orcid.org/0000-0002-7344-9920

Mahito Sasada ● https://orcid.org/0000-0001-5946-9960

Tuomas Savolainen ● https://orcid.org/0000-0001-6214-1085

Lijing Shao ● https://orcid.org/0000-0002-1334-8853

Zhiqiang Shen (沈志强) ● https://orcid.org/0000-0003-3540-8746

Des Small ● https://orcid.org/0000-0003-3723-5404

Bong Won Sohn ● https://orcid.org/0000-0002-4148-8378

Jason SooHoo ● https://orcid.org/0000-0003-1938-0720

He Sun (孙赫) ● https://orcid.org/0000-0003-1526-6787

Fumie Tazaki ● https://orcid.org/0000-0003-0236-0600

Alexandra J. Tetarenko ● https://orcid.org/0000-0003-3906-4354

Paul Tiede ● https://orcid.org/0000-0003-3826-5648

Remo P. J. Tilanus ● https://orcid.org/0000-0002-6514-553X

Michael Titus ● https://orcid.org/0000-0002-3423-4505

Kenji Toma ● https://orcid.org/0000-0002-7114-6010

Pablo Torne ⓘ https://orcid.org/0000-0001-8700-6058
Efthalia Traianou ⓘ https://orcid.org/0000-0002-1209-6500
Sascha Trippe ⓘ https://orcid.org/0000-0003-0465-1559
Ilse van Bemmel ⓘ https://orcid.org/0000-0001-5473-2950
Huib Jan van Langevelde ⓘ https://orcid.org/0000-0002-0230-5946
Daniel R. van Rossum ⓘ https://orcid.org/0000-0001-7772-6131
Jan Wagner ⓘ https://orcid.org/0000-0003-1105-6109
Derek Ward-Thompson ⓘ https://orcid.org/0000-0003-1140-2761
John Wardle ⓘ https://orcid.org/0000-0002-8960-2942
Jonathan Weintroub ⓘ https://orcid.org/0000-0002-4603-5204
Norbert Wex ⓘ https://orcid.org/0000-0003-4058-2837
Robert Wharton ⓘ https://orcid.org/0000-0002-7416-5209
Qingwen Wu (吴庆文) ⓘ https://orcid.org/0000-0003-4773-4987
Doosoo Yoon ⓘ https://orcid.org/0000-0001-8694-8166
André Young ⓘ https://orcid.org/0000-0003-0000-2682
Ken Young ⓘ https://orcid.org/0000-0002-3666-4920
Ziri Younsi ⓘ https://orcid.org/0000-0001-9283-1191
Feng Yuan (袁峰) ⓘ https://orcid.org/0000-0003-3564-6437
Ye-Fei Yuan (袁业飞) ⓘ https://orcid.org/0000-0002-7330-4756
J. Anton Zensus ⓘ https://orcid.org/0000-0001-7470-3321
Guang-Yao Zhao ⓘ https://orcid.org/0000-0002-4417-1659
Shan-Shan Zhao ⓘ https://orcid.org/0000-0002-9774-3606

References

Bardeen, J. M., Press, W. H., & Teukolsky, S. A. 1972, ApJ, 178, 347
Blackburn, L., Chan, C.-k., Crew, G. B., et al. 2019, ApJ, 882, 23
Blackburn, L., Pesce, D. W., Johnson, M. D., et al. 2020, ApJ, 894, 31
Bronzwaer, T., Davelaar, J., Younsi, Z., et al. 2018, A&A, 613, A2
Chan, C.-k., Psaltis, D., & Özel, F. 2013, ApJ, 777, 13
Chan, C.-k., Psaltis, D., Özel, F., Narayan, R., & Sądowski, A. 2015, ApJ, 799, 1
Christian, P., & Psaltis, D. 2020, AJ, 159, 226
Event Horizon Telescope Collaboration, Akiyama, K., Alberdi, A., et al. 2019a, ApJL, 875, L1
Event Horizon Telescope Collaboration, Akiyama, K., Alberdi, A., et al. 2019b, ApJL, 875, L2
Event Horizon Telescope Collaboration, Akiyama, K., Alberdi, A., et al. 2019c, ApJL, 875, L3
Event Horizon Telescope Collaboration, Akiyama, K., Alberdi, A., et al. 2019d, ApJL, 875, L4
Event Horizon Telescope Collaboration, Akiyama, K., Alberdi, A., et al. 2019e, ApJL, 875, L5
Event Horizon Telescope Collaboration, Akiyama, K., Alberdi, A., et al. 2019f, ApJL, 875, L6
Gammie, C. F., McKinney, J. C., & Toth, G. 2003, ApJ, 589, 444
Gebhardt, K., Adams, J., Richstone, D., et al. 2011, ApJ, 729, 119
Gravity Collaboration, Abuter, R., Amorim, A., et al. 2019, A&A, 625, L10
Igumenshchev, I. V., Narayan, R., & Abramowicz, M. A. 2003, ApJ, 592, 1042
Janssen, M., Goddi, C., van Bemmel, I. M., et al. 2019, A&A, 626, A75
Jennison, R. C. 1958, MNRAS, 118, 276
Kulkarni, S. R. 1989, AJ, 98, 1112
Leung, P. K., Gammie, C. F., & Noble, S. C. 2011, ApJ, 737, 21
Medeiros, L., Chan, C.-k., Özel, F., et al. 2017, ApJ, 844, 35
Medeiros, L., Chan, C.-k., Özel, F., et al. 2018, ApJ, 856, 163
Mościbrodzka, M., Falcke, H., & Shiokawa, H. 2016, A&A, 586, A38
Mościbrodzka, M., & Gammie, C. F. 2018, MNRAS, 475, 43
Narayan, R., Sądowski, A., Penna, R. F., & Kulkarni, A. K. 2012, MNRAS, 426, 3241
Olivares Sánchez, H., Porth, O., & Mizuno, Y. 2018, JPhCS, 1031, 012008
Porth, O., Chatterjee, K., Narayan, R., et al. 2019, ApJS, 243, 26
Psaltis, D. 2019, GReGr, 51, 137
Psaltis, D., Medeiros, L., Christian, P., et al. 2020, PhRvL, 125, 141104
Roelofs, F., Johnson, M. D., Shiokawa, H., Doeleman, S. S., & Falcke, H. 2017, ApJ, 847, 55
Sądowski, A., Narayan, R., McKinney, J. C., & Tchekhovskoy, A. 2014, MNRAS, 439, 503
Sądowski, A., Narayan, R., Penna, R., & Zhu, Y. 2013, MNRAS, 436, 3856
Thompson, A. R., Moran, J. M., & Swenson, G. W. J. 2017, Interferometry and Synthesis in Radio Astronomy (3rd ed.; Berlin: Springer)
Walsh, J. L., Barth, A. J., Ho, L. C., & Sarzi, M. 2013, ApJ, 770, 86
Wielgus, M. & The Event Horizon Telescope Collaboration 2020, ApJ, 901, 67